Bulletin of Earthquake Engineering (2026) 24:4875–4911
https://doi.org/10.1007/s10518-025-02328-1

ORIGINAL ARTICLE

Numerical modeling of the out-of-plane dynamic response of masonry gable walls via a high-fidelity block-based finite element modeling approach – part I: Blind prediction

Amirhossein Ghezelbash[1] · **Antonio Maria D'Altri**[2] · **Paulo B. Lourenço**[3] · **Stefano de Miranda**[2]

Received: 31 May 2025 / Accepted: 17 November 2025 / Published online: 26 February 2026

Abstract

This paper deals with the blind prediction of the dynamic out-of-plane (OOP) response of unreinforced masonry gables via block-based modelling within a competition organized by ERIES SUPREME. Three gable wall specimens were tested at the EUCENTRE foundation in Pavia, Italy, under incremental shaking-table earthquake loading until collapse. In the tests, each wall was subjected to distinct boundary conditions, simulating interactions with stiff, flexible, and semi-flexible diaphragms. The competition challenged participants to predict the responses of two of these walls, replicating stiff and flexible diaphragms, with minimal access to experimental data and outcomes, emphasizing the need for reliable modeling techniques. The authors utilize a novel 3D block-based model, originally developed for cyclic quasi-static responses and recently extended to dynamic one- and two-way OOP bending. Both the walls and the loading set-up are simulated. The masonry assembly of the walls is conceived as solid expanded blocks connected via zero-thickness planar joints in the former. The robustness of the predictions is enhanced through a sensitivity analysis exploring the influence of variations in mechanical properties, vertical and dynamic loading assumptions, and damping on the response. Numerical models predict the key experimental observations, such as the collapse onset, failure mechanisms, displacement demands, and dynamic responses, with good accuracy, achieving the best blind prediction results. Indeed, the modeling approach shows great capability to capture complex dynamic interactions, highlighting its potential in complementing physical testing. Moreover, the simulation is able to successfully predict not only the global response of the gables, but also to reproduce several details affected by the test set-up and loading assumptions. The modeling strategy appears a good candidate for sensitivity and probabilistic analysis, capable of extending the current understanding of seismic performance in masonry structures and overcoming limitations inherent in experimental methods.

Keywords Unreinforced masonry · Numerical modeling · Seismic loading · Out-of-Plane · Gable walls · Blind prediction

Extended author information available on the last page of the article

1 Introduction

Unreinforced masonry structures (URM) are among the most widely used forms of construction globally, owing to their accessibility, affordability, and ease of implementation (Hendry 2001). These structures, constructed from readily available materials, are commonly employed in both historic and contemporary buildings across diverse regions (Frankie, Gencturk and Elnashai 2013). However, despite their advantages, masonry walls are characterized by limited tensile strength and brittle out-of-plane failure mechanisms, which make them particularly vulnerable to dynamic loads such as those induced by earthquakes (Frankie, Gencturk and Elnashai 2013). This inherent vulnerability poses significant challenges to ensuring the seismic safety of masonry structures, particularly in regions with high seismicity (D'Ayala and Paganoni 2011; Moon et al. 2014; Oyarzo-Vera and Griffith 2009; p. 1991; Penna et al. 2014). As a result, substantial research efforts have been devoted to investigating their seismic performance in an experimental setting.

Since most research focuses on the seismic response of URM walls under in-plane loading, the out-of-plane (OOP) response of these structures remains an aspect not sufficiently explored (D'Ayala and Paganoni 2011; Sorrentino et al. 2016). Moreover, while invaluable contributions have been made to understanding the one-way and two-way bending OOP behaviors or single and return walls in a dynamic setting (Candeias et al. 2016; Giaretton, Dizhur and Ingham 2016; Graziotti et al. 2019; Griffith et al. 2004; Moshfeghi et al. 2024; Penner and Elwood 2016b; Simsir and Aschheim 2004; Vaculik and Griffith 2018), not much attention is given to more complex geometries such as gables typical of low-rise buildings commonly found worldwide. Moreover, current state-of-the-art experiments rarely account for the role of realistic boundary conditions, such as interaction between the walls and floor diaphragms, on the OOP dynamic response due to physical constraints of the test set-ups (Penner and Elwood 2016a; Sharma et al. 2021; Tomassetti et al. 2019; Tondelli, Beyer and DeJong 2016).

To address the need for advancing the understanding of seismic OOP responses in URM gable walls, and to bridge the gap between experimental observations and real-world seismic demands, the Seismic Out-of-Plane Response of Masonry Gables (SUPREME) campaign is conceived within the scope of the EU-funded transnational access programme Engineering Research Infrastructure for European Synergies (ERIES) and is conducted at the EUCENTRE foundation, Pavia, Italy. Within the campaign, also referred to as ERIES SUPREME, the performance of full-scale masonry gables subjected to different boundary motions simulating interactions with stiff, flexible, and semi-flexible diaphragms is investigated in multi-step incremental dynamic shake table tests (Sharma et al. 2025). Additionally, a blind prediction competition is organized, motivated by the need to evaluate and enhance numerical modeling approaches for capturing the complex seismic behavior of URM gable walls.

Various numerical approaches exist for modeling the dynamics of masonry, ranging from simplified macro-element (Kesavan and Menon 2023; Malomo and DeJong 2022; Vanin, Penna and Beyer 2020) and continuum-based (Lourenço 2000; Noor-E-Khuda 2021; Noor-E-Khuda, Dhanasekar and Thambiratnam 2016; Rots et al. 2016; Selby and Vecchio 1993), to multi-scale (Sharma et al. 2021) and detailed block-based (D'Altri et al. 2018; Furiosi et al. 2025; Kesavan and Menon 2022; Macorini and Izzuddin 2011; Malomo, Pinho and Penna 2020; Mohyeddin, Goldsworthy and Gad 2013; Nie et al. 2023; Oktiovan et al. 2024, 2024; Xie et al. 2021) ones. Numerical approaches provide a cost-effective alternative to physical tests, enabling dynamic simulations of masonry under different loading scenarios with reduced costs and time, accommodating complex boundary conditions and full-scale structures that are often unfeasible in laboratory settings. However, rigorous calibration is essential for numerical models to align with real-world observations, especially those of complex multi-step dynamic experiments. Without it, critical behaviors like failure mechanisms and seismic responses may be misrepresented, compromising prediction reliability. Validation against experimental benchmarks is, therefore, indispensable to ensure accuracy and practical relevance (Girardi et al. 2021; Lourenço 2004).

To address the need for a reliable and effective numerical modeling approach, a block-based numerical modeling framework was developed in (Ghezelbash et al. 2024) for the high-fidelity analysis of the dynamic OOP behaviors in URM walls. The approach, originally developed for quasi-static studies in (D'Altri et al. 2019), was extended to the dynamic regime in (Ghezelbash et al. 2024) to reproduce the one-way bending behavior of URM walls under sequential shake table loading. The model was then further extended to two-way bending incremental dynamic test simulations in (Ghezelbash et al. 2025), proving to be a reliable complement to experiments in expanding the current knowledge to scenarios not studied previously.

In this study, the aforementioned modeling approach is adopted to blind-predict the outcomes of the experiments conducted within the ERIES SUPREME campaign, further showcasing its reliability and effectiveness in producing accurate estimation of real-world responses even without knowledge of the actual recorded behaviors. The current paper focuses on the activities carried out during the blind prediction phase of the study, including the numerical modeling activities carried out in the scope of the competition and the outcomes of the prediction simulations. A second article will report on the adjustments considered for the numerical models in the post-diction phase, the extension of numerical modelings to the third wall not part of the blind prediction, and subsequent investigations carried out to extrapolate the knowledge acquired during the experiments to walls with different roof/wall connections and pre-damages. The content of the current paper is organized as follows. Section 2 introduces the tests considered for the blind prediction and the limited experimental data made available to the participants at the time of the competition. The step-by-step procedure adopted by the authors to generate numerical models solely based on those data is detailed in Section 3. The parametric study, formulated to account for the uncertainties governing experimental settings and to approach the problem from a statistical point of view, is explained in Section 4. The results of the numerical simulations are presented in Section 5 and systematically compared against the experimental outcomes that were made available only after the competition. Finally, the main findings of the paper, along with recommendations for potential future research, are presented in Section 6.

2 Description of the experiments and the data published for the competition

This section provides a brief overview of the experimental campaign (Graziotti et al. 2024; Sharma et al. 2025) used as the reference for the blind prediction competition. The campaign is performed at the EUCENTRE foundation (Pavia, Italy) and investigates the dynamic behavior of unreinforced masonry gable walls subjected to incrementally increasing shake table earthquake loads applied at their top and bottom boundaries. To replicate various wall-roof interaction scenarios, three sets of boundary conditions are employed (Mirra et al. 2025): (1) similar motions at the top and bottom of the wall to represent stiff roof diaphragms such as reinforced concrete, (2) different motions at the top and bottom to simulate the effects of flexible roof diaphragms such as timber, and (3) an intermediate condition reflecting semi-flexible diaphragms such as retrofitted timber. The competition focuses on the first two cases, described in this section. To reflect the conditions under which the blind-prediction competition was conducted, the experimental information presented herein is limited to those made available to the contestants during the competition. Specifically, the loading sequence described in Section 2.3 corresponds to the sequence provided to the participants for the blind-prediction simulations, rather than the actual sequence used in the experiments. More in-depth discussion of the actual experimental programme based on the data published after the competition is presented Section 5 to demonstrate the performance of the predictions of the authors.

2.1 Test-set up

The experimental set-up is depicted in Fig. 1. Each gable wall specimen measures 3 m in height and 6 m in length, constructed as a single-leaf unreinforced masonry structure. Each wall consists of 45 courses of clay bricks, each measuring 23.0 × 5.5 × 10.5 cm (length ×2 height × thickness), with 1.0 cm thick lime-based mortar joints in a stretcher bond configuration. Each wall is in the form of an isosceles triangle. The walls are laid on a regular mortar bed joint placed on a pre-stressed reinforced concrete foundation bolted to the shake table. The top motion is applied to a thick steel slab supported by four steel columns placed on the shake table. The motion is transferred to the walls via a frame and joist system made of steel.

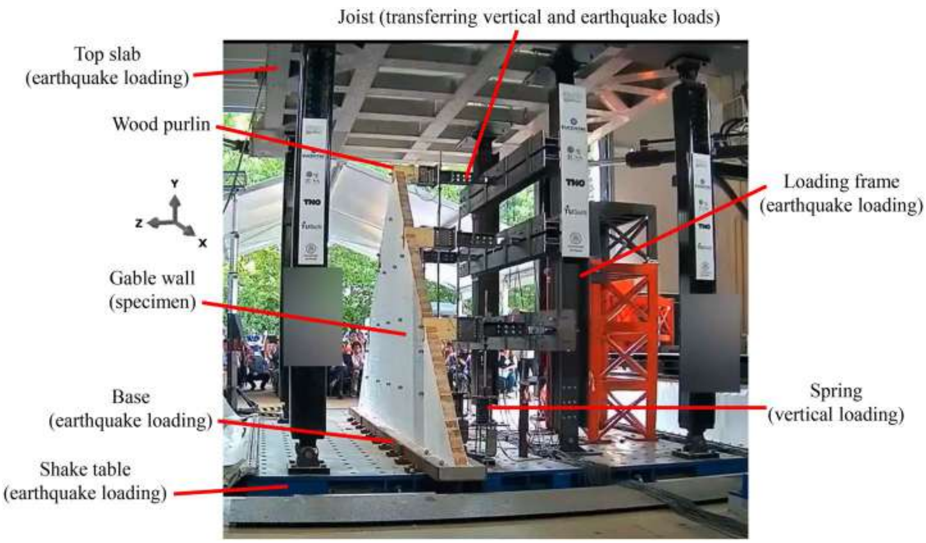

Fig. 1 Overview of the experimental set-up used to test the gable walls in the ERIES supreme experimental campaign (Sharma et al. 2025). This figure was published during the blind prediction competition and belongs to the specimen not included in the competition

The frame comprises two HEB300 steel columns with a 3 m center-to-center spacing and three rows of beams, each consisting of double-HEB180 profiles stacked horizontally. The joists, 76 cm in length, connect to a 30 cm-long C24-grade timber purlin. The purlins, 20 cm in height, connect the joists to the walls at different elevations. Specifically, five wedges are cut in the walls above the 15th, 30th, and 43rd rows of bricks to house the purlins in a dry-joint friction-only connection. The wedges are 10 cm long and three bricks high, with a 0.5–1.0 cm gap between the vertical edges of the timbers and the internal wedge surfaces. A dry mortar layer is applied at the bottom face of each wedge before placing the purlins. Vertical loads are applied via spring and rod assemblies connected to each joist at a 46 cm offset from the wall face. For the numerical modeling purposes of this study, the walls are assumed to lie in the x-y plane, with the y-axis pointing upward and the z-axis extending outward from the loading frame. Cylindrical hinge connections at the table and top slab connections with the loading frame and the columns allow the slab and table to displace in the z-direction while permitting the rotation of the columns and loading frame about the x-axis. The vertical hinge-to-hinge height of the loading frame is 3.735 m, with the bottom hinge aligned with the wall base joint. Similar hinges connect the joists to the frame with a 36 cm offset from the frame column faces. Each vertical rod is pinned to its joist, allowing free relative rotation about the x-axis, while the bottom of the loading springs can rotate freely in all directions, akin to spherical hinges. Purlins are secured to the joists via steel enclosures and high-strength bolts. Bolt connections are also employed to construct the loading frame. The frame, joists, and all connecting elements are overdesigned to behave nearly rigidly, minimizing amplification effects on the motion transferred to the wall and ensuring that top and bottom motions remain consistent.

2.2 Input motions

Dynamic loading for each specimen is conducted using two sets of acceleration time histories (Mirra et al. 2025): one representing an induced-seismicity event and another from a tectonic event. The former set is derived from a numerical model of a terraced house typical of the Groningen area in the Netherlands (Mirra, Ravenshorst and van de Kuilen 2020), subjected to a representative earthquake for that region related to gas extraction (Bommer et al. 2015). The tectonic signal is generated using a single degree of freedom model of the same building, under accelerograms extracted from a school building during a central Italy earthquake (Graziotti et al. 2019). For the experiments, the accelerations "applied" to the gable walls are extracted from the attic and roof of these numerical models. The accelerations "recorded" by the shake table and top slab accelerometers during loading runs corresponding to 100% intensity of the applied induced and tectonic loading signals are shown in Fig. 2 ("i" set of images). These accelerograms are processed in this study via a third-order bandpass Butterworth filter (0.2–50 Hz) and linear baseline correction to remove sensor-induced electrical noise and to have their resulting displacements match the recorded ones (Boore and Bommer 2005). In the "Flexible-Diaphragm" test (referred to as "Flexible" test or the case under "Differential" boundary motions), each set consists of two distinct acceleration time histories, one applied to the shake table and one to the top slab. In contrast, the "Stiff-Diaphragm" test (referred to as "Stiff" test or the case under "Equal" boundary motions) assumes identical base and top motions, though minor discrepancies arise due the challenges in keeping the two motions identical during the experiments. The spectral content

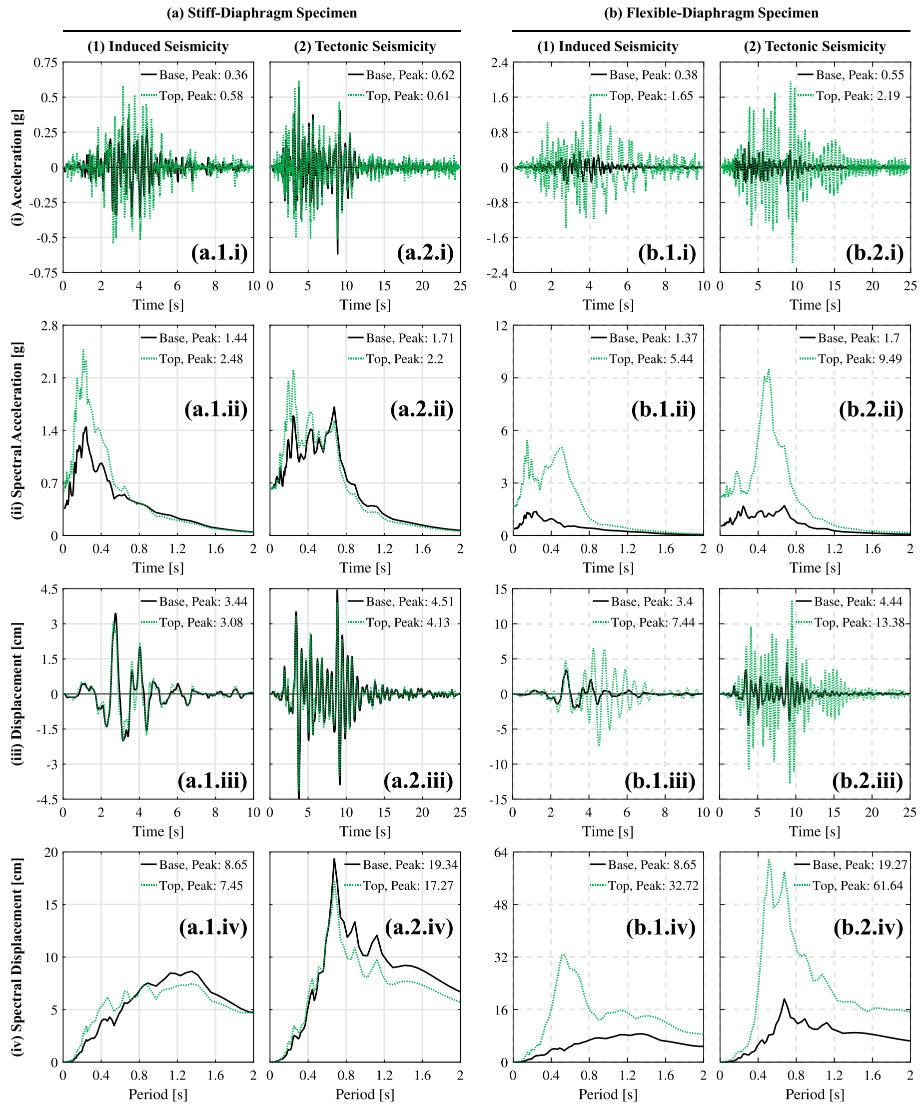

Fig. 2 Boundary motions recorded during the benchmark tests. Each row of subfigures is dedicated to acceleration (**i**) and displacement (iii) time histories and 5%-damped acceleration (ii) and displacement (iv) spectra of the motions. The motions recorded during stiff-diaphragm (**a**) and flexible-diaphragm (**b**) experiments are shown in separate two-column sub-figures. The two columns of each experiments show the motions recorded during induced (1) and tectonic (2) seismicity loading runs at 100% intensity. Only this information was published during the blind prediction competition. The motions processed in this study are shown instead of the raw data

of the accelerograms as well as the time history and spectral content of their displacements are shown in Fig. 2.ii, Fig. 2.iii, and Fig. 2.iv, respectively. The subfigures are ordered so that the two left columns (Fig. 2.a) show the signals from the Stiff-Diaphragm experiment and the two right columns (Fig. 2.b) show the signals from the Flexible-Diaphragm test. In each two-column set, the right column (Figure 2.1) shows the induced seismicity signal and the left column (Figure 2.2) shows the tectonic seismicity signal. It should be noted that the processed loading signals shown in the figure are only minorly different from the raw signals provided in the competition data in terms of acceleration, displacement, and spectral content. Hence, the illustration of the raw data together with these processed signals is avoided for the sake of clear visualization.

2.3 Loading sequences

The loading sequence outlined in Table 1 was used for both the Stiff and Flexible cases during the blind-prediction competition. Each wall was initially subjected to a vertical load of 4 kN in each timber purlin, followed by a sequence of dynamic inputs. This sequence included six loading runs using induced-seismicity signals and additional runs with tectonic-seismicity signals, with the intensity incrementally increased based on the scale factors listed in Table 1 until collapse occurred. The Stiff case utilized the signals shown in Fig. 2.a.i, while the Flexible case employed the signals from Fig. 2.b.i. The organizers proposed extending the sequence if collapse was not reached by the end of the 16 runs presented here by adding additional runs wherein the signal intensity increased in each run by a scale factor 0.5 higher than that of the preceding run. It should be noted that the 4 kN vertical load applied at each purlin-wall connection was later updated to 4.5 kN in the experimental data published after the competition (Sharma et al. 2025). However, this more accurate value was not available to participants during the competition, and therefore, a value of 4 kN was used in the simulations. The implications of this discrepancy will be discussed in the second part of this study.

Table 1 Loading sequence published for numerical modeling during the blind prediction competition

Run Number (N)	Input Motion Type	Scale Factor (SF_N)	Peak Base Acceleration	
			Stiff Test	Flexible Test
Gravity load on entire geometry with $g=9.81\ m/s^2$				
4 kN vertical load transferred by each timber purlin				
1	Induced Seismicity	0.10	0.036 g	0.038 g
2	Induced Seismicity	0.20	0.072 g	0.076 g
3	Induced Seismicity	0.30	0.108 g	0.114 g
4	Induced Seismicity	0.50	0.180 g	0.190 g
5	Induced Seismicity	0.75	0.270 g	0.285 g
6	Induced Seismicity	1.00	0.360 g	0.380 g
7	Tectonic Seismicity	0.50	0.310 g	0.275 g
8	Tectonic Seismicity	0.75	0.465 g	0.413 g
9	Tectonic Seismicity	1.00	0.620 g	0.550 g
10	Tectonic Seismicity	1.25	0.775 g	0.688 g
11	Tectonic Seismicity	1.50	0.930 g	0.825 g
12	Tectonic Seismicity	1.75	1.085 g	0.963 g
13	Tectonic Seismicity	2.00	1.240 g	1.100 g
14	Tectonic Seismicity	2.50	1.550 g	1.375 g
15	Tectonic Seismicity	3.00	1.860 g	1.650 g
16	Tectonic Seismicity	3.50	2.170 g	1.925 g
N+1	Tectonic Seismicity	$SF_N+0.5$	–	–

3 Numerical modeling procedure

An overview of the 3D numerical model used to predict the experimental outcomes is presented in Fig. 3. The model includes a simplified representation of the loading frame, joists, foundation, vertical loading system, and a detailed replication of the gable walls. For simplicity, the shake table, top slab, and supporting columns are excluded. However, the remaining elements of the loading set-up are incorporated to capture amplification effects arising from motion transfer through the back frame and joists. The vertical loading system is also explicitly modeled to account for variations in vertical loads caused by joist rotation and vertical movement. This section outlines the modeling procedure, including the generation of geometries (Section 3.1), simulation of the masonry walls (Section 3.2), connection between different parts of the models (Section 3.3), mechanical characterization of the numerical loading set-up (Section 3.4), finite element discretization scheme (Section 3.5), prescribed boundary conditions (Section 3.6) and loading protocol (Section 3.7), and the approach used to analyze the structures in dynamics (Section 3.8). The numerical model was created with the Abaqus finite element analysis software (Hibbitt, Karlsson and Sorensen 2011).

3.1 Geometry and dimensions

The detailed geometrical dimensions of different parts of the models are depicted in Fig. 4. The positioning of the wall and loading frame is done assuming the same global coordinate system defined for the experimental set-up in Fig. 1, i.e., z-axis oriented towards the front of the wall. Although the steel profiles of the loading frame are replaced with solid rectangular members to reduce computational demands, key dimensions, including the height

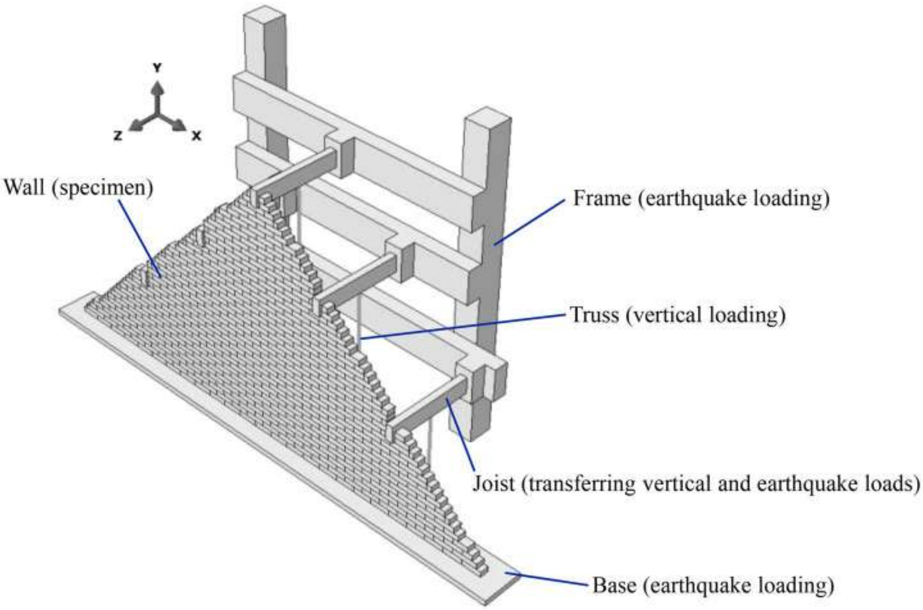

Fig. 3 Overview of the numerical model produced for the gable walls

and horizontal spacing of the columns, the length and vertical spacing of the beams, and their outer cross-sectional dimensions, are preserved. The procedure for equalizing the mass and stiffness of the idealized numerical steel members to that of the profiles used in the experimental set-up is explained in Section 3.4. The offset between the joists and frame is achieved by attaching solid parts to the beams. The joists are modeled as rectangular prisms, their first 76 cm (towards the frame) as steel and the remaining 30 cm (towards the walls) as timber. Masonry walls are represented (according to Section 3.2) using 45 courses of $24.0 \times 6.5 \times 10.5\,cm^3$ expanded blocks (extended in length and height to account for the 1 cm thickness of the mortar layers) and zero-thickness joints, resulting in numerical specimen dimensions close to experimental ones. To prevent excessive computational demand, the wall sides are shaped with half- and quarter-blocks instead of fine-cut slopes, as such detailing has negligible influence on the performance of the walls. Wall-to-joist connections are modeled with wedges at the elevations matching the experimental set-up. The joist cross-section ($8.6 \times 19.5\,cm^2$) allows for a 0.7 cm gap on either side of the wedges and maintains the experimental three-brick row height. The numerical wall is placed at a distance from the loading frame consistent with the experimental set-up, with an additional 2.5 cm of timber protruding in front to ensure stability during large relative motions. The concrete foundation is replaced with a solid 6.5-cm-thick rectangular base on each side of the walls to accommodate wall-base slipping. The vertical loading system is modeled with five pre-stressed truss members, each connected to its joist at a 47 cm offset from the joist-frame connection.

3.2 Modeling the masonry walls

The block-based modeling approach developed in (Ghezelbash et al. 2024, 2025) for high-fidelity dynamic analysis of one- and two-way bending OOP behavior of URM walls, is employed for simulating the gables. This method represents masonry using expanded blocks and zero-thickness joints, depicted in Fig. 5.a, offering a meso-scale (or simplified micro-scale) representation. Expanded blocks, modeled as nonlinear continuum solid bodies, follow the isotropic Concrete Damaged Plasticity (CDP) model developed in (Lee and Fenves 1998; Lubliner et al. 1989), representing compressive behavior of masonry wal-

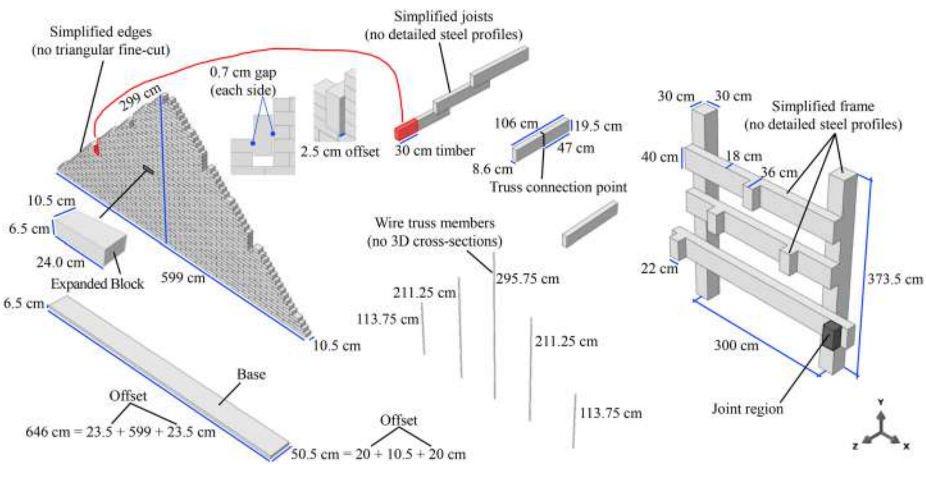

Fig. 4 Geometrical dimensions of the numerical model constituents

lets and tensile response of masonry units. Zero-thickness joints are modeled with a planar master-slave contact algorithm (Hibbitt, Karlsson and Sorensen 2011; Weyler et al. 2012) and capture tensile and shear failures of the mortar and unit-mortar interface, with tensile responses being cohesive and shear responses cohesive-frictional. Non-dilatant behavior is assumed for the joints, with dilatancy effects incorporated into the block response according to a non-associative plastic flow rule.

Simplified constitutive behaviors of the blocks and the joints, adopted for computational efficiency according to (Ghezelbash et al. 2024, 2025), are also depicted in Fig. 5. The compressive response in blocks includes a post-peak plateau followed by linear softening, while their tensile response exhibits post-peak linear softening (Fig. 5.b), similarly to the shear-cohesive (blue curve in Fig. 5.c) and tensile (Fig. 5.d) responses of the joints. The joints are also assigned a constant-friction shear response (green curve in Fig. 5.c). Residual strengths of 10% are applied to the post-softening compressive and tensile responses of the blocks to prevent numerical divergence. Under cyclic loading, blocks exhibit elastic unloading during the compressive plateau phase and reduced stiffness proportional to damage during softening. Their compressive and tensile behaviors are coupled, where prior damage in one mode affects the strength and stiffness in the other. Joints display secant unloading-reloading behavior in the normal direction and elastic stiffness in combined shear cohesive-frictional responses. The multiaxial behavior of blocks follows the Drucker-Prager multi-yield surface (Lee and Fenves 1998), while the shear response of the joints is assumed isotropic in-plane. More details of the constitutive cyclic responses can be found in (Ghezelbash et al. 2024).

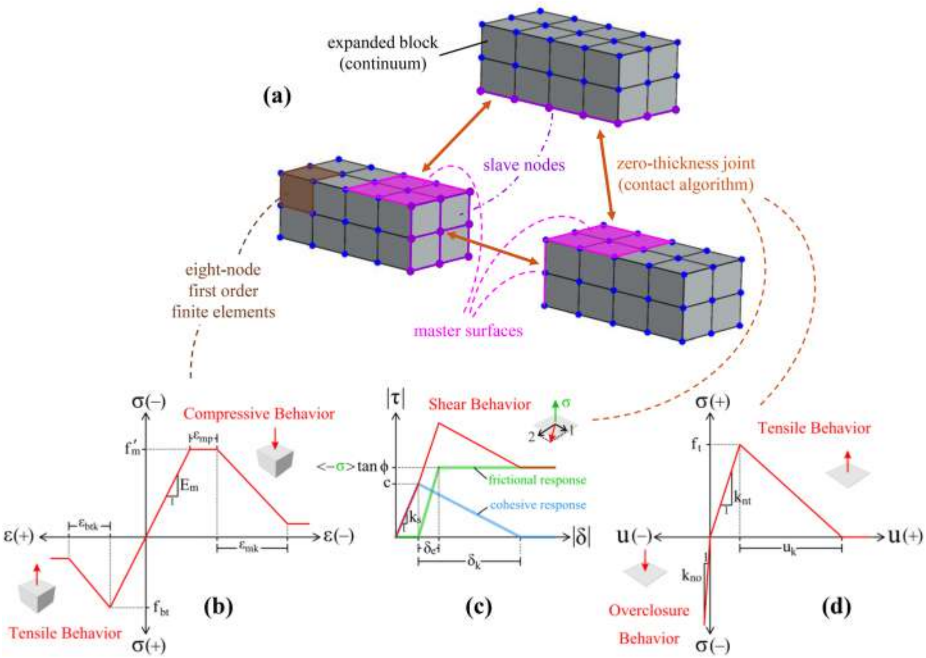

Fig. 5 Block-based approach used for the modeling of the gable walls: overview of the constituents (**a**), the uniaxial compressive-tensile response of the expanded blocks (**b**), and shear (**c**) and (**d**) normal response of the zero-thickness joints. Cyclic behaviors are detailed in (Ghezelbash et al. 2024)

The input parameters for the expanded blocks and joints are calibrated using the approach proposed in (D'Altri et al. 2019), which links material-level small-scale test results to structural-level simulations. However, since small-scale test data for the materials used in the gable wall construction were unavailable, the average material properties published by the organizers of the blind prediction competition were adopted directly. Table 2 lists these input parameters, with bold values representing those provided by the organizers for the competition and other values, such as those for the post-peak response of the blocks and the joints, assumed based on typical masonry behaviors (Jafari, Esposito and Rots 2019) as well as previous works of the authors (Ghezelbash, Messali and Rots 2023). Parameters for blocks include the elasticity modulus (E_m), compressive strength (f'_m), and density (ρ_m) of masonry wallets, tensile strength of the masonry units (f_{bt}), and the lengths of compressive plateau (ε_{mh}), as well as compressive (ε_{mk}) and tensile (ε_{btk}) softening regimes. Additional parameters, such as masonry wallet Poisson's ratio (ν_m), dilatancy angle (ψ), and CDP model coefficients (i.e., eccentricity $\in$, biaxial to uniaxial compressive strength ratio f_{b0}/f_{c0}, and stress invariant ratio ρ_{CDP}), are based on values commonly used for quasi-brittle materials (Jafari and Esposito 2016; Lubliner et al. 1989; Milani, Valente and Alessandri 2018; Scacco et al. 2020). Joint parameters include overclosure stiffness (k_{no} assumed large to avoid block interpenetration), cohesive stiffnesses in tension (k_{nt} assumed equal to normal overclosure stiffness for simplicity) and shear (k_s), and elastic slip (δ_e), friction coefficient ($\tan\phi$), cohesion (c), and tensile strength of the unit-mortar bond (f_t taken as the ⅔ of masonry bond wrench strength f_w), and softening lengths in tension (u_k) and shear (δ_k). No distinction is made between head and bed joints, as it is assumed that head joints are completely filled and exhibit similar strength to bed joints.

3.3 Assembling the model

The connections between components in the numerical model, including frame-joist, truss-joist, purlin-wall, and wall-base connections, are illustrated in Fig. 6. Each frame-joist cylindrical hinge connection is replicated via two reference points located at the center of the joist end (on the frame side) cross-section. One reference point is coupled to a 6-cm-long section of the frame joint via kinematic coupling in all degrees of freedom (DoFs) (Yue,

Table 2 Input parameters for the mechanical behavior of the masonry gable wall. Bold values are from experimental data published during the competition. The parentheses indicate the CoV of the reported values

Expanded blocks							
Elastic behavior		Plasticity parameters		Compressive behavior		Tensile behavior	
E_m [MPa]	**4072 (11%)**	ψ [°]	10	f'_m [MPa]	**7.44 (10%)**	f_{bt} [MPa]	2.0
ν_m [−]	0.17	$\in$ [−]	0.1	ε_{mp} [−]	0.002	ε_{btk} [−]	0.001
Density		f_{b0}/f_{c0} [−]	1.16	ε_{mk} [−]	0.012		
ρ_m $[kg/m^3]$	**2000 (NA)**	ρ_{CDP} [−]	2/3				
Zero-thickness joints							
Overclosure behavior		Tensile cohesive behavior		Shear cohesive behavior		Shear frictional behavior	
k_{no} $[N/mm^3]$	241.4	k_{nt} $[N/mm^3]$	241.4	k_s $[N/mm^3]$	103.1	$\tan\phi$ [−]	**0.42 (NA)**
		f_t [MPa]	**0.18 (44%)**	c [MPa]	**0.21 (NA)**	δ_e [mm]	0.01
		u_k [mm]	0.6	δ_k [mm]	0.6		

Fafitis and Qian 2010), while the other is similarly coupled to the 6-cm-long end of the joist. These reference points are then linked through kinematic coupling in all DoFs except for rotation about the x-axis. Each truss connects to its respective joist via a reference point placed at its top node, aligned with the center of a joist cross-Sect. 47 cm away from the frame-joist hinge. Kinematic coupling in translational DoFs links the truss top to the reference point, simulating a spherical hinge. A 6-cm-long region of the joist is coupled to the reference point (3 cm offset on either side of the point). This configuration prevents over-constraint in rotational DoFs and ensures only axial loads are transferred from the trusses to the joists. Purlin-wall and wall-base connections use the contact algorithm described in Section 3.2. The purlin-wall connection employs friction-only contact with high overclosure stiffness, whereas the wall-base connection employs regular mortar contact properties.

3.4 Test set-up characterization

The simplified test set-up in the numerical models is calibrated to replicate the elastic response and inertial properties of its experimental counterpart, ensuring the reproduction of boundary conditions and dynamic amplification effects as accurately as possible. The input parameters for the mechanical behavior of the set-up and the input parameters adopted for them are detailed in Fig. 7 and Table 3, respectively. The loading frame is modeled using an isotropic elastic material. Based on steel profile information extracted from (European Committee for Standardization 2005), mass and stiffness equivalency with the experimental frame are achieved to closely match its modal behavior and frequencies during OOP motions. The steel portions of the joists and hinge regions are similarly modeled. The base is modeled as an isotropic elastic component using properties of the gable wall blocks, and its rigid behavior is ensured through the boundary condition couplings described in Section 3.6. Each truss is calibrated to match the stiffness of its corresponding experimental vertical loading spring (53.5 N/mm, adopted from the past experimental campaigns conducted at EUCENTRE (Graziotti et al. 2016, 2019)). Pre-stressing is applied via thermal loading, with the thermal expansion coefficient of each truss calibrated to produce the desired verti-

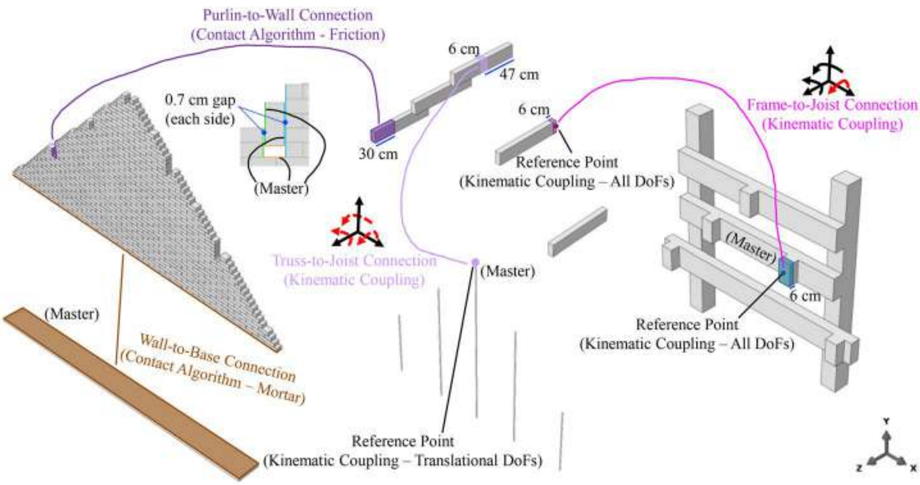

Fig. 6 Connections between different constituents of the models

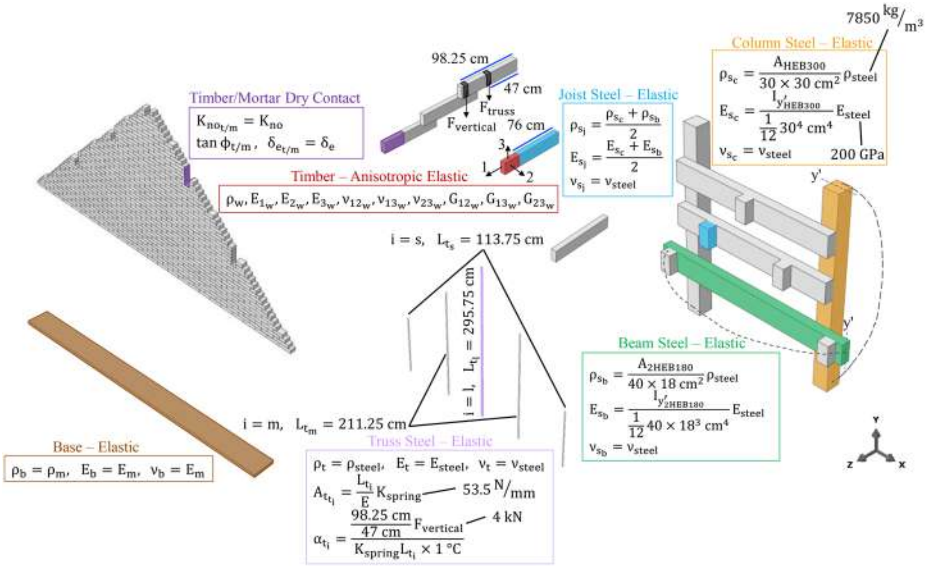

Fig. 7 Mechanical behavior assigned to the simulated test set-up

Table 3 Input parameters for the Mechanical characterization of the numerical test set-up

Frame and Joist Steel Parts						Base	
Columns		Beams		Hinge Regions and Joists			
E_{s_c} [GPa]	74.58	E_{s_b} [GPa]	78.83	E_{s_j} [GPa]	76.71	E_b [GPa]	4072
ν_{s_c} [−]	0.30	ν_{s_b} [−]	0.30	ν_{s_j} [−]	0.30	ν_b [−]	0.17
ρ_{s_c} $\left[kg/m^3\right]$	1300	ρ_{s_b} $\left[kg/m^3\right]$	1422	ρ_{s_j} $\left[kg/m^3\right]$	1361	ρ_b $\left[kg/m^3\right]$	2000
Vertical Trusses						Purlin/Wall Connection	
Elastic Behavior		Cross-Section Area		Thermal Behavior			
E_t [GPa]	200	A_{t_s} $\left[mm^2\right]$	0.3046	α_{t_s} [−]	0.1345	$K_{no_{t/m}}$ $\left[N/mm^3\right]$	241.4
ν_t [−]	0.3	A_{t_m} $\left[mm^2\right]$	0.5691	α_{t_m} [−]	0.0724	$\tan\phi_{t/m}$ [−]	0.60
ρ_t $\left[kg/m^3\right]$	7850	A_{t_l} $\left[mm^2\right]$	0.7951	α_{t_l} [−]	0.0519	$\delta_{e_{t/m}}$ [mm]	0.001
Purlin Timber Parts							
Elasticity Moduli		Poisson's Ratios		Shear Moduli		Density	
E_{1_w} [MPa]	11000	ν_{12_w} [MPa]	0.50	G_{12_w} [MPa]	690	ρ_w $\left[kg/m^3\right]$	420
E_{2_w} [MPa]	370	ν_{13_w} [MPa]	0.45	G_{13_w} [MPa]	690		
E_{3_w} [MPa]	370	ν_{23_w} [MPa]	0.45	G_{23_w} [MPa]	60		

cal load (4 kN) at the purlin-wedge connections upon a 1 °C temperature drop. Purlin-wall connections are modeled with the same overclosure stiffness and elastic slip as the gable wall joints, while their timber/mortar friction coefficient ($\tan\phi_{t/m}$) is assumed to be 0.6 as the lower-bond value reported in the experimental studies of (Almeida et al. 2020). The timber portions of the joists are modeled as anisotropic elastic materials, with principal axes aligned to the longitudinal (z), vertical (y), and lateral (x) directions of the joists and input parameters for C24 timber sourced from (The British Standard 2003; Eslami, Jayasinghe and Waldmann 2021; European Committee for Standardization 2004). The use of an anisotropic material model for the timbers is preferred over isotropic models for two main reasons. First, the response of the gables is expected to be highly sensitive to the purlin-wall connections, and even minor deviations from the actual geometry or behavior of the timbers, such as the simplifying assumption of using an isotropic material, may result in significantly different dynamic responses. Second, in the experiments, the timbers may have deformed in a manner that allowed interaction with the walls at their vertical edges, thereby contributing to additional horizontal confinement of the gables. An anisotropic material model is expected to more accurately capture such deformations and the real bending stiffness of the timbers along their principal axes.

3.5 Finite element discretization

The numerical model components are discretized into eight-node hexahedral solid elements with linear shape functions. A standard element size of 6 cm is applied throughout, with finer meshing assigned to critical regions for increased accuracy, as shown in Fig. 8. Specific areas, including offsets at the sides, top, and bottom of the loading frame, the joist ends, joist-truss connections, and the thickness of the base, are divided into two rows of elements. This prevents element distortion or under-constraining in coupling connections described in Sections 3.3 and 3.6. Truss members are each discretized into a single element along their height to ensure proper truss-like behavior and avoid hypo-elasticity. For the masonry expanded blocks, a $4 \times 1 \times 2$ (length×height×thickness) discretization is adopted, which is deemed sufficient to capture one-way bending responses. However, refinements are also made in specific critical regions. To enhance the wall-purlin connections, the blocks around purlins are given three elements in thickness, those blocks adjacent to purlins are divided into two elements in height, and those half-blocks beneath purlins have two elements in length. Accordingly, the timber purlins are discretized into six elements in their height, three elements over their length in contact with the wedge, and four elements in their cross-sectional thickness, which aligns their mid-thickness nodes with mid-length nodes of

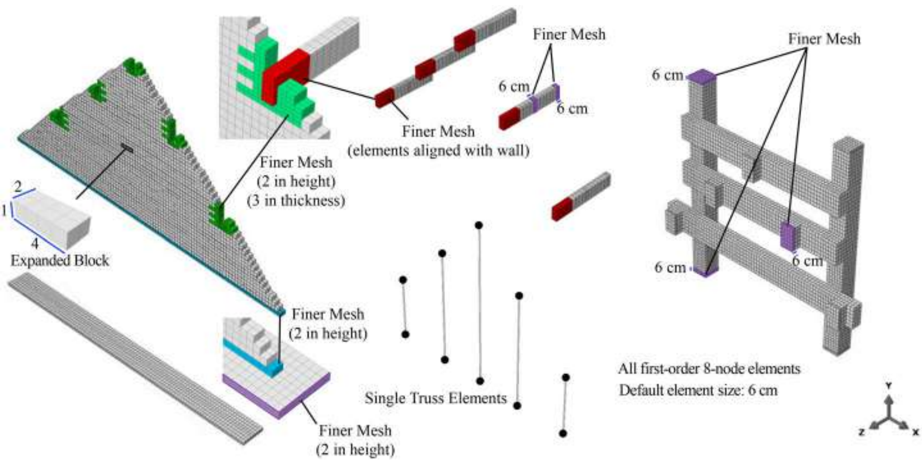

Fig. 8 Finite element discretization adopted for the numerical models

underlying blocks. To properly capture compression effects, the blocks beneath purlins and the first row of blocks at the base of the wall are given two elements in height.

3.6 Boundary conditions

The boundary constraints of the numerical models, depicted in Fig. 9, are designed to replicate the experimental set-up. The top and bottom ends of each column in the loading frame are connected to reference points at their free cross-section centers. At the bottom, all degrees of freedom (DoFs) are fixed except rotation about the x-axis, prescribing a cylindrical hinge motion. The top reference points are similarly constrained, except allowing vertical translation along the y-axis to simulate slab movement caused by column rotation. Stiff kinematic coupling connects the column ends to the reference points, transferring deformations as prescribed by the master points. The wall base is coupled to a reference point at its geometrical center, fixed in all DoFs. Truss bottoms are slaved to reference points at their location through translational DoFs only, allowing free rotational motion akin to a spherical hinge connection.

3.7 Loading protocol

The loading sequence follows Table 1. Gravitational acceleration ($g = 9.81\,m/s^2$) is first applied, followed by thermal loading where the temperature of the trusses is reduced by 1 °C for them to pre-stress and generate the 4 kN vertical load at each purlin-wall connection. Unlike direct vertical load application, this vertical loading method accounts for second-order effects and load variations due to wall deformations. It also does not alter the frequency of the models, contrary to techniques such as using concentrated masses. Dynamic earthquake loading is then applied following the published sequence until the collapse of the walls is reached in the form of cracking and physical instability. Signals shown in Fig. 2.i are applied opposite to the positive direction of the z-axis, as per the benchmark tests, and are scaled to different intensities for different loading runs. The base, truss-bottom, and frame-bottom reference points are subjected to base motions, while top motions are

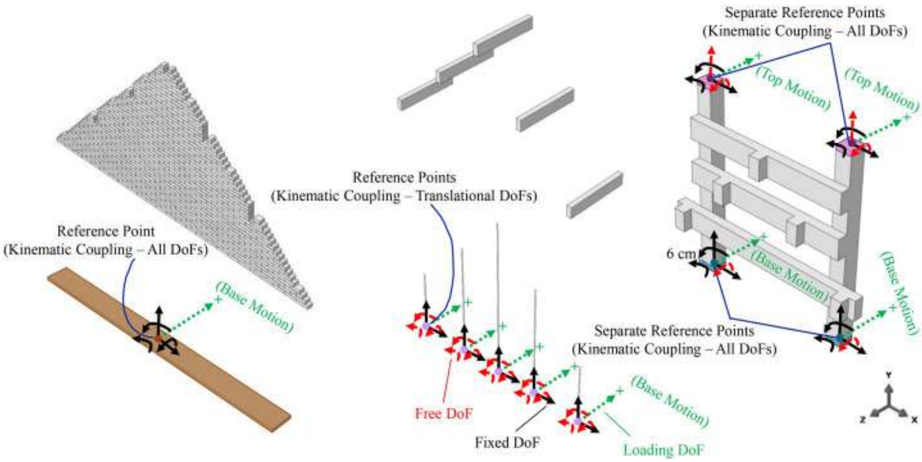

Fig. 9 Boundary and loading conditions adopted in the numerical models

applied to frame-top reference points. The complete accelerogram time histories of the signals are applied to include the repositioning of the walls before and after high-intensity portions. Only, approximately the final 0.3 seconds of the signals are removed as preliminary analyses revealed them to lead to mismatches between the displacements of top and bottom boundaries at the end of the signals, causing cumulative residual OOP drift in the loading frame and tilting of the walls not observed in experiments. The 0.3 seconds threshold varies between each set of loading signals and has been identified by manually inspecting the loading signals and finding the last moment in which the top and base slabs reach the same displacement value. After each dynamic loading run, the specimens are allowed to rest in a static step for the stresses to properly propagate and to inspect the residual damages. Modal analysis is performed after gravity, vertical, and dynamic loading steps, and after resting periods between runs, to monitor the natural frequencies of the walls and track the progression of damage.

3.8 Dynamic solver and damping

Following (Ghezelbash et al. 2024), the dynamic loading runs in the numerical models are performed with the implicit Hilbert-Hughes-Taylor (HHT) direct integration solver (Hilber, Hughes and Talor 1977), adopting minimal numerical damping ($\alpha_{\mathrm{HHT}} = -0.05$) and automatic time-stepping with a maximum increment size matching the sampling rate of the experimental (0.00391 s). The latter also allows for a one-on-one comparison of numerical outputs against experimental recordings. Rayleigh damping is applied to the expanded blocks to model dynamic energy dissipation, using both mass- and stiffness-proportional components. The Rayleigh damping input parameters are calculated from the natural frequencies of the models (see Section 5.1) and assuming a 5% target damping ratio (ζ_{R}) across the geometry. This damping ratio, validated in prior work by the authors (Ghezelbash et al. 2024, 2025), is well-suited for modeling the one-way and two-way dynamic out-of-plane responses of masonry under incremental seismic loading sequences. The latter is proven in the previous works of authors (Ghezelbash et al. 2024, 2025) as a suitable value for the simulation of one-way and two-way bending dynamic out-of-plane responses in URM walls.

4 Investigation of variations in numerical model parameters

To gain deeper insights into the dynamic behavior of the specimens and account for uncertainties inherent in experimental studies and dynamic responses, several additional variations are simulated for each test, as outlined in Table 4. Despite the high computational demands (232 hours for the Stiff case and 197 hours for the Flexible case on average using 16 CPU cores @ 4.2 GHz clock speed), thirteen variations are here selected for each scenario. Each variation is designated as “Vi”, where “i” represents the variation number. The baseline simulations, V1, employ the set-up described in Section 2, with elastic blocks in the purlin-wall connection regions to prevent numerical divergence due to stress concentrations causing distortion and loss of contact at the blocks underneath the timber element. Since V1 produced failure mechanisms solely involving zero-thickness joints and the purlin-wall connections (see Section 5.2), the possibility of reproducing the same responses by assuming elastic blocks across the walls is investigated in V2 variations. As such endeavor was successful, and indeed the results of V1 and V2 were substantially identical, elastic behavior is assumed for all blocks of the subsequent variations, increasing computational efficiency and avoiding numerical problems.

Joint properties, specifically the tensile strength (f_t), is recognized as a critical parameter due to its influence on failure mechanisms (as previous studies (Ghezelbash et al. 2025) show) and a high variability (44%) in masonry bond strength (f_w) was reported in the published experimental data. Variations V3 and V4 explore the effects of f_t by adopting 25% lower and higher values, respectively. The cohesive-shear strength (c) and softening branch lengths (u_k and δ_k) in joints are kept the same as the reference models. It is expected that the timber/mortar friction coefficient ($\tan\phi_{t/m}$) also significantly affects dynamic load transfer and wall stability, while no experimental information regarding this parameter was published in the competition data. Hence, V5 and V6 variations using 25% lower and higher $\tan\phi_{t/m}$values (still within the experimental range reported in (Almeida et al. 2020)) are considered for further investigation. The possibility of the experimental loading set-up showing lower stiffness (K_{frame}) due to looseness of beam and frame connections is investigated in V7 variations by halving the elastic moduli of the frame and joists. Similarly, V8 examines the effects of increased vertical truss stiffness (K_{truss}) as the loading springs used in the tests may have shown larger stiffness compared to their nominal properties. Such is achieved by enlarging truss cross-sections by 25%. The thermal coefficients of trusses are scaled accordingly to maintain the intended 4 kN vertical load at purlin-wall connections. To assess the impact of vertical load variability due to the elongation and rotation of the springs, V9 replaces the trusses with constant downward concentrated forces at the truss/joist connections. In V10, shake table motions are identically applied to the top and bottom boundaries to investigate response sensitivity to discrepancies in experimental input. The influence of the loading direction on the response is examined by applying signals in the

Table 4 Different numerical variations considered for the sensitivity study

Variation	Masonry Properties		Purlin/Wall Connection		Loading Set-Up		Loading Assumptions		Damping
	Blocks	Joints f_t	Blocks	$\tan\phi_{t/m}$	K_{frame}	K_{truss}	Vertical	Earthquake	ζ_R
V1	**Nonlinear**	100%	Linear	100%	100%	100%	Truss	Original	5%
V2	Linear	100%	Linear	100%	100%	100%	Truss	Original	5%
V3	Linear	**75%**	Linear	100%	100%	100%	Truss	Original	5%
V4	Linear	**125%**	Linear	100%	100%	100%	Truss	Original	5%
V5	Linear	100%	Linear	**75%**	100%	100%	Truss	Original	5%
V6	Linear	100%	Linear	**125%**	100%	100%	Truss	Original	5%
V7	Linear	100%	Linear	100%	**50%**	100%	Truss	Original	5%
V8	Linear	100%	Linear	100%	100%	**125%**	Truss	Original	5%
V9	Linear	100%	Linear	100%	100%	–	**Point Load**	Original	5%
V10[i]	Linear	100%	Linear	100%	100%	100%	Truss	**Base Motion**	5%
V11	Linear	100%	Linear	100%	100%	100%	Truss	**Reverse Direction**	5%
V12	Linear	100%	Linear	100%	100%	100%	Truss	Original	**3%**
V13	Linear	100%	Linear	100%	100%	100%	Truss	Original	**7%**

Considered only for the Stiff specimen: base motion is applied to all (top and bottom) boundaries positive z-axis direction, reversing the reference model set-up explained in Section 3.7. Finally, damping sensitivity is explored in V12 and V13 by adjusting the target Rayleigh damping ratio (ζ_{R}) to 3 and 7%, respectively.

5 Results and discussion

This section presents the outcomes of blind prediction numerical simulations and assesses the performance of the numerical models against experimental observations published after the competition. While the competition primarily required predictions of failure mechanisms and collapse-inducing loading intensities, additional key responses are examined. Section 5.1 discusses the modal analysis of the walls at the onset of simulations. Failure mechanisms and the loading runs associated with the collapse of each specimen are detailed in Section 5.2. Displacement demands recorded in various regions of the models are discussed in Section 5.3, and the sliding behavior between timber purlins and their adjacent bricks is analyzed in Section 5.4. The effectiveness of the numerical loading set-up is evaluated in Section 5.5 by analyzing the amplification effects of the loading frame on dynamic motions experienced at the wall-purlin connections. The variations in the vertical load of the trusses are evaluated in Section 5.6. Finally, Section 5.7 explores hysteretic response and energy dissipation of each model, offering insights into the effectiveness of the damping strategy (see Section 3.8) in simulating dynamic behaviors. In each section, the V1 variations of both Stiff and Flexible cases (see Table 4) are assumed as the reference models representing the predicted behavior of the experiments and are used to check the performance of other variations.

5.1 Modal analysis

Modal analysis is performed at the start of the simulations to determine the natural vibration modes and frequencies of the models and to calibrate the Rayleigh damping parameters of the blocks. Figure 10.a illustrates the modal shapes, while Fig. 10.b and Fig. 10.c present the natural frequencies and participating mass factors for each mode of vibration, respectively. The data of all numerical variations are shown with blue circle markers, except for V7 models (with 50% reduced frame stiffness) which exhibit slightly different results as shown with red lines and square markers. V7 models maintain the same sequence and pattern of natural vibration modes as other variations, indicating no significant deviation in the frame behavior. However, V7 models display slightly lower modal frequencies, with the first mode reduced by 10%, and the more significant difference being an 18% reduction in the frequency of the fifth mode. Participating mass factors for V7 also show minor deviations from the other models, with a combined 12% higher participation in the fourth and sixth modes. These results suggest that the original frame stiffness is sufficiently high to have only a minor impact on the response, even if halved. Moreover, V7 specimens and the rest of the numerical models show first mode frequencies very close to the 25.7 Hz frequency extracted from the post-processing of the experimental data published after the competition, shown via a green star marker in Fig. 10.b. Thus, the numerical loading set-up is rigid and aligns well with the experimental test set-up, a topic explored further in Section 5.5. To ensure consistency, Rayleigh damping calibration is done using the first and fourth natural frequencies, with the latter included to account for its slight mass participation in

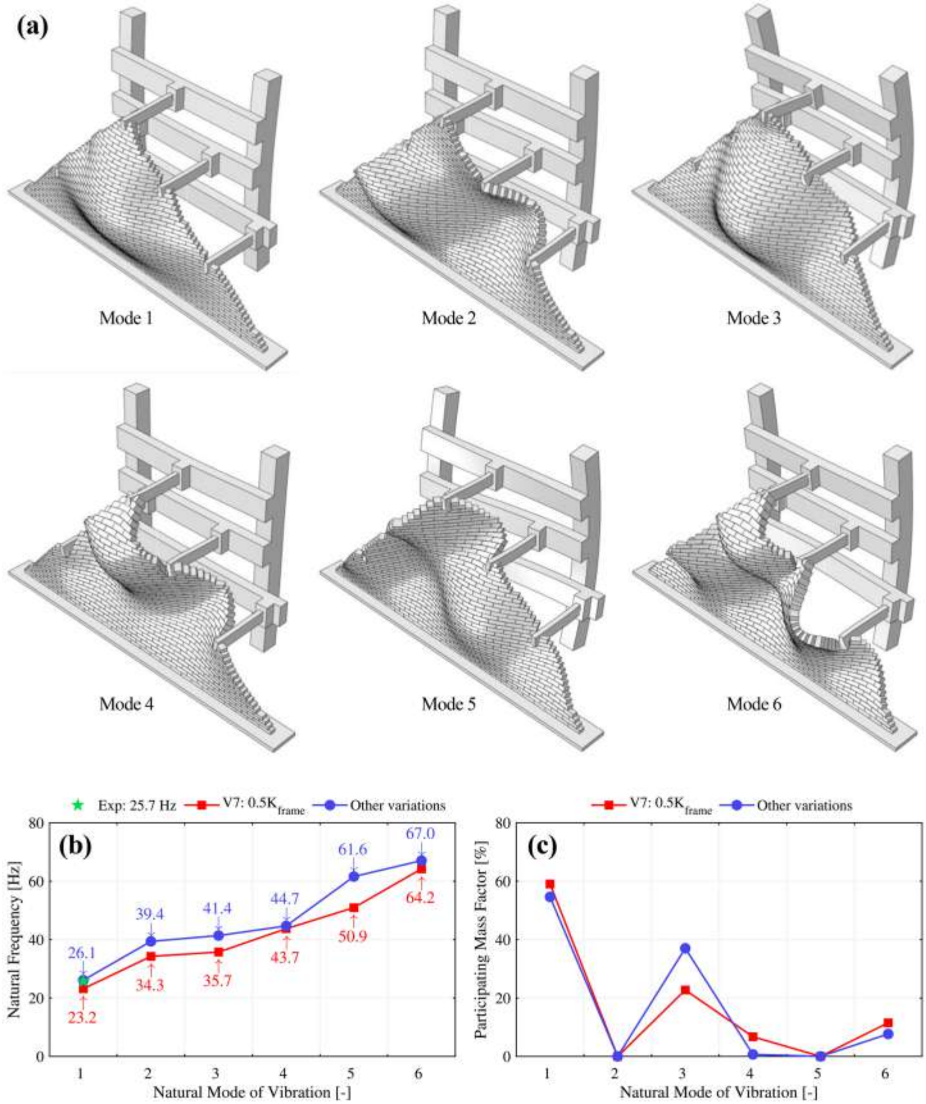

Fig. 10 The results of the modal analysis of the numerical walls: modal shapes (**a**), frequencies (**b**), and participating mass factors (**c**) of the first six natural modes of vibration. Experimental data were published only after the competition

the response of V7 models. Higher modes are excluded due to their high frequencies (above 60 Hz) and minimal expected influence.

5.2 Collapse onset and failure mechanism

Figure 11 shows the loading intensities corresponding to the collapse of each numerical model and its reference experimental outcome in terms of peak base acceleration (PBA).

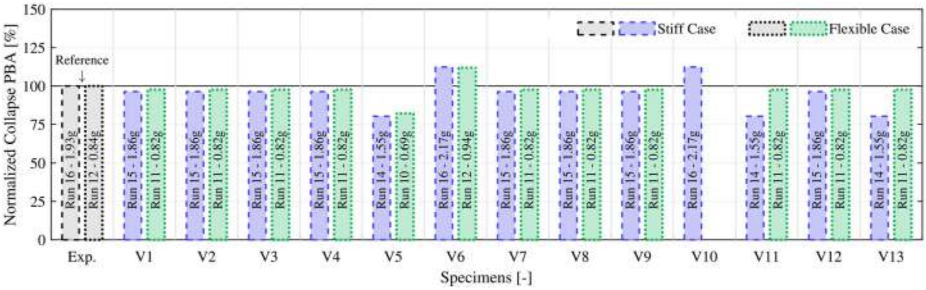

Fig. 11 Loading runs and peak base accelerations (PBAs) corresponding to the collapse of the experimental and numerical specimens. Experimental data were published only after the competition

The bars of each specimen (being Stiff with dashed edges and Flexible with dotted edges) are normalized to the experimental data (gray bars) for the sake of comparison with numerical results (blue bars for Stiff and green bars for Flexible specimens). In the experiments and the numerical models, collapse is identified as the inability of the wall to return to equilibrium conditions at the end of the dynamic loading run, i.e., physical instability that results in the falling of the entire or parts of the wall specimens. For the Stiff case, collapse occurs at loading run 16 in the experimental test under loading signals with PBA of 1.93 g. Most numerical variations, including the reference V1 model, provide close predictions of the response, collapsing at a PBA of 1.86 g, which is 4% lower, but in one loading run before the experiment. Variations V6 (increased purlin-wall connection friction) and V10 (base motion applied at all boundaries), predict collapse at run 16, similar to the experiment, but with a 12% higher PBA (2.17 g). The rest of the variations (V5 with decreased purlin-wall connection friction, V11 with reversed loading direction, and V13 with increased damping), collapse earlier at run 14 with a PBA of 1.52 g, which is 20% lower than the experimental one. In the Flexible case, the experimental wall collapses at loading run 12, with peak accelerations of 0.82 g and 3.28 g recorded at the top and bottom shake tables. Numerical models, including the reference V1, generally replicate this behavior, with the same loading intensities but at one earlier loading run. Only variations V5 (decreased purlin-wall connection friction) and V6 (increased purlin-wall connection friction) deviate slightly by collapsing at loading runs 10 and 12, respectively, under 14% lower and higher PBAs.

The numerical models effectively predict the loading intensities corresponding to the collapse of the specimens, with a maximum difference of 20% between the experimental and numerical peak base accelerations (PBAs). This deviation is considered minor and falls within the expected uncertainties inherent to dynamic conditions in experimental settings. While most models predict collapse one loading run earlier than observed experimentally, their PBAs align closely with the recorded values, attributed to distinct reasons for the Stiff and Flexible cases. For the Stiff case, the numerical collapse intensity at run 15 corresponds with the experimental PBA reported at run 16. This outcome arises from how loading intensities are computed numerically. Specifically, the PBAs are calculated by scaling the processed reference signals from Fig. 2.i using the scale factors in Table 1. These processed signals differ from the raw experimental data due to overshooting or undershooting effects inherent to the shake table as well as the filtering adopted herein, leading to slight discrepancies between the motions experienced in the experiments and those assumed in the numerical models. In simple words, while the experimental Stiff specimen experiences a peak base acceleration (PBA) of 1.93 g during its loading run 16, the Stiff walls simulated in this study reach a very similar PBA of 1.86 g already during loading run 15. This occurs because the loading signals used in the numerical simulations are not identical to those recorded during the experiments, but rather are processed versions of them. In the Flexible case, the numerical PBA at run 11 matches the experimental PBA at run 12 due to an additional induced seismicity run being included in the experimental loading sequence. This extra run, not previously disclosed in the competition experimental data, causes the experimental sequence to extend by one additional run compared to the numerical setup.

The cracking patterns and damage progressions recorded in the Stiff and Flexible experiments are shown in Fig. 12. Both specimens show one-way bending failure mechanisms with horizontal cracks forming at their base as well as 1/3-height and 2/3-height elevations. While the Stiff specimen shows maximum deformation at 1/3-height, with the top portion of the wall remaining less deformed until collapse, the peak deformations of the Flexible specimen occur close to the 2/3-height elevation. This, suggesting the effects of distinct loading conditions considered for each specimen, is also evident in the damage progression of the walls: while the 2/3-height crack occurs as early as three loading runs before the collapse of the Flexible wall, it only appears at near collapse conditions in the Stiff specimen (one run before collapse). It should also be noted that cracking of the mortar layer at the base of both walls initiates at loading intensities well below those associated with collapse, since this region experiences the highest rotational moments and consequently largest tensile stresses due to OOP deformations. Moreover, no crushing is observed in the bricks underneath the timber element at purlin-wall connections or other regions of the walls, confirming the feasibility of adopting elastic blocks across the numerical models.

The different types of collapse mechanisms observed across numerical models are depicted in Fig. 13. The deformed shapes are magnified with different scales for clear visualization. As such, the purlin-wall detachments, except in Fig. 13.e and Fig. 13.f are artificial and a result of scaled deformed shapes. The failure mechanisms of the Stiff models primarily align with the experimental one-way bending response. However, the numerical cracks

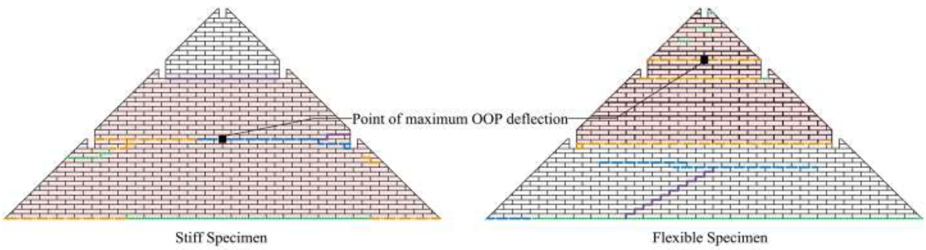

Damage State:	DS1 (Light Damage)	DS2 (Moderate Damage)	DS3 (Severe Damage)	DS4 (Near Collapse)	DS5 (Collapse: One-Way Bending)
Stiff Test:	Loading Run 4 (Induced, PBA: 0.19g)	Loading Run 13 (Tectonic, PBA: 1.17g)	Loading Run 14 (Tectonic, PBA: 1.51g)	Loading Run 15 (Tectonic, PBA: 1.88g)	Loading Run 16 (Tectonic, PBA: 1.93g)
Flexible Test:	Loading Run 7 (Tectonic, PBA: 0.28g)	Loading Run 8 (Tectonic, PBA: 0.43g)	Loading Run 9 (Tectonic, PBA: 0.57g)	Loading Run 11* (Induced, PBA: 0.70g)	Loading Run 12** (Tectonic, PBA: 0.85g)

* Corresponds to Run 10 in the numerical models ** Corresponds to Run 11 in the numerical models

Fig. 12 Failure mechanisms and crack progressions observed in the experiments of Stiff and Flexible specimens along with identified damage states and their corresponding loading runs. The figure is drawn based on the information published after the competition (Sharma et al. 2025) do not precisely reflect the experimental ones. In most models, including V1, cracks only appear at the base and beneath the 2/3-height purlins (Fig. 13.a). Variations such as V4 (with higher tensile strength for joints), V5 (with lower purlin-wall connection friction), V10 (base motion applied to both top and bottom of the loading set-up), and V12 (with lower damping) show a better prediction of the location of maximum deformations, with the base crack accompanied by cracking at the 1/3-height elevation (Fig. 13.b). V7 (with halved frame stiffness) and V9 (with point force for vertical loading) models show the closest match with the experimental crack pattern, with the major cracks at base, 1/3-, and 2/3-height elevations all forming in these variations (Fig. 13.c and Fig. 13.d). The V11 model (under reversed loading direction) shows the most inaccurate failure mechanism in the form of overturning (Fig. 13.e). For the Flexible case, the experimental failure mechanism is not captured sufficiently. The models predominantly show an overturning failure mechanism with base cracking, followed by the detachment of the purlins (Fig. 13.e). Amongst different variations, only the one with a stronger purlin-wall connection (V6) shows additional cracking at 1/3-height elevation (Fig. 13.f), yet the detachment of purlins still prevents the formation of a more complete collapse mechanism.

The variations of failure mechanisms discussed above highlight the sensitivity of the dynamic response to a variety of parameters as well as the ability of the models to explore potential deviations in experimental failure mechanisms under slightly altered conditions.

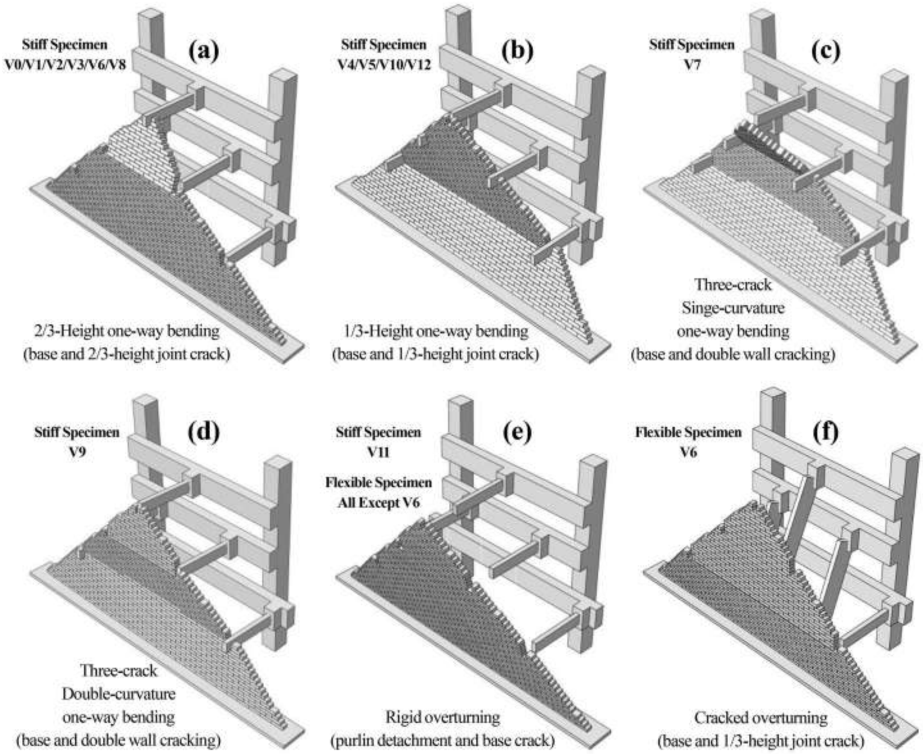

Fig. 13 Failure mechanism types observed in the numerical models: all Stiff variations (**a**) except V4 and V5 and V10 and V12 (**b**), V7 (**c**), V9 (**d**), and V11 (**e**), as well as all Flexible variations (**e**), except V6 (**f**). The deformed shapes are magnified with different scales for clear visualization

The possible factors contributing to the discrepancies between numerical and experimental cracking patterns are identified as follows:

- The use of sample loading signals to excite the specimens at different loading runs instead of adopting the actual motions experienced by the walls during different runs of the tests is believed to be one of the contributors especially for the Flexible case. As investigated in the preliminary analyses not discussed in this paper, as well as shown in the V10 variation for the Stiff specimen, slight changes in the input motions, even low-amplitude high-frequency noises, can significantly affect the outcome of dynamic simulations. The influence of loading signals on the behavior of the gables is further explored in the second part of this study.
- The testing set-up conceived for the numerical models, especially the vertical loading apparatus and its connection with the walls (purlin-wall connection friction coefficient), is another factor controlling the response of the Flexible and Stiff specimens, respectively (see Section 5.4).
- The inherent limitations of the adopted implicit solver in capturing during- and post-collapse responses could have also prevented the simulation of the entire failure mechanisms of each specimen. Aside from the base crack, which forms at the same loading runs observed in the experiments, the rest of the cracks in the numerical models only begin to form in the final loading runs (except for the V3 Stiff model, where they form in run 13). However, the simulations using an implicit solver, as done in this study, typically proceed only until excessive deformation of the walls during the first cracking (such as in the Stiff case) or the detachment of different parts (such as purling from the Flexible specimen). It is believed that had certain simulations proceeded further, they may have shown cracking more consistent with the experiments.

The first and third factors could not be explored further during the prediction phase due to the lack of access to the rest of the motion data from experiments and time constraints, respectively. However, the second factor involving a parametric study on different modeling assumptions is pursued, and the results are discussed in the next subsections.

5.3 Observed displacements

The maximum out-of-plane displacements (relative to base) recorded at different elevations of the walls in both Stiff and Flexible numerical models are compared against experimental outputs in Fig. 14. The experimental data are shown with black solid curves, and the numerical data from V1 reference models and the V3 and V4 variations, featuring 25% lower and higher joint tensile strength (f_t), respectively, are depicted with dashed blue, dotted red, and dashed-dotted green lines, respectively. The collapse of the specimens is highlighted via cross-marks (×).

Although the numerical models track the experimental data with good accuracy in the loading runs prior to collapse, they show larger differences in the final loading runs. This is not unexpected given the high sensitivity of the displacements close to collapse runs. In V1 numerical models of both Stiff and Flexible cases, the highest displacements occur at the top of the walls, as shown in Fig. 14.iii, whereas their corresponding experiments show peak displacements at the 1/3- and 2/3-height elevations, respectively. The Stiff model col-

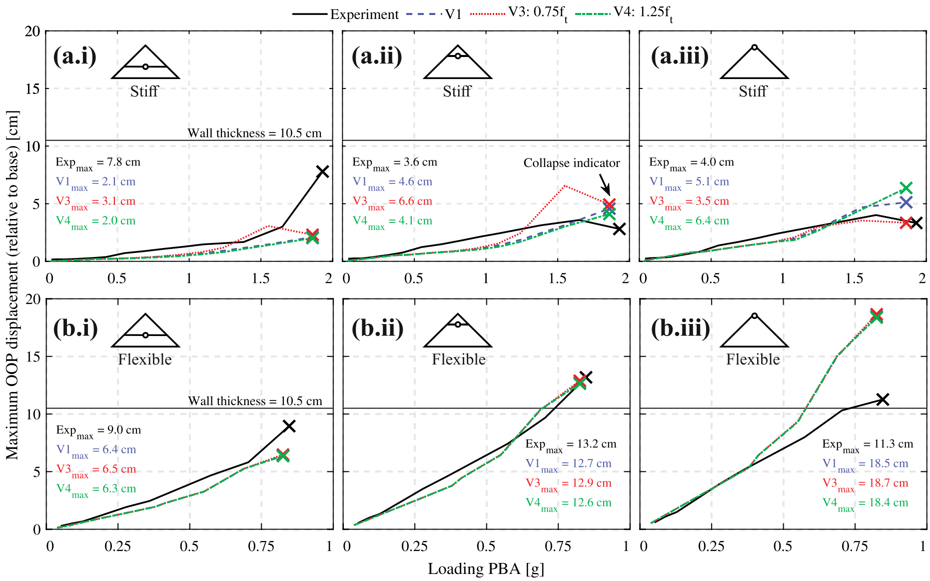

Fig. 14 Maximum OOP displacements recorded during different loading runs: data from the 1/3-height (**i**), 2/3-height (ii), and 3/3-height (iii) elevations in the Stiff-Diaphragm (**a**) and Flexible-Diaphragm (**b**) specimens. Experimental data were published only after the competition. The variations, the data of which is not shown, demonstrate comparable levels of displacement

lapses with a maximum top drift of 5.1 cm (close to half its thickness), which is close to the 7.8 cm displacement observed in the experiment, yet appears at a different location. In Flexible case, while the 2/3-height elevation of the model shows similar displacements to the tested wall, its top shows an 18.7 cm displacement (80% larger than its thickness and 60% larger than the experimental value). This greater stability is attributed to the large relative deformation of the top boundary with respect to the base (16.6 cm) and the support provided by the joists, as well as the cracking not being activated in the numerical wall. For the Stiff numerical model, the 2/3-height elevation exhibits displacements similar to the top, consistent with the one-way bending mechanism dominated by a crack opening at that level. Conversely, the Flexible wall shows more pronounced differences in drifts between the top and 2/3-height, indicative of the influence of its overturning mechanism.

In the Stiff V3 variation, reduced joint tensile strength causes early crack formation at the 2/3-height in loading run 13, increasing displacement demands thereafter. However, collapse occurs in the same loading run 15 as in the V1 model due to confinement provided by the joists. Similarly, the Flexible V3 variation collapses at the same run as V1, despite earlier cracking, and due to the delay provided by the joists. The increased tensile strength in V4 variations has minimal effect on collapse loading runs but alters the failure mechanism in the Stiff case, where cracking shifts to the 1/3-height elevation. In conclusion, changes in tensile strength influence the damage onset and failure mechanism in the Stiff case but have negligible effects on the Flexible case, where behavior across variations remains largely consistent.

5.4 Sliding between purlins and the walls

The maximum relative out-of-plane displacements (referred to as sliding) between the timber purlins and their adjacent blocks during different loading runs of Stiff and Flexible specimens are illustrated in Fig. 15. Experimental data are shown with solid black lines, and the numerical data from V1 reference models and the V5 and V6 variations with 25% lower and higher friction adopted at purlin-wall connections ($\tan\phi_{t/m}$) are shown with dashed blue, dotted red, and dashed-dotted green lines, respectively. The 13 cm detachment threshold shown in the figures is characterized as the summation of the thickness of the walls (10.5 cm) and the additional 2.5 cm offset assumed for the timbers. In the case of outward movement of the walls, sliding values above this threshold indicate the complete separation of the specimens from the purlins, such as in Fig. 13.e and Fig. 13.f.

In the experiments, peak sliding values of 5.1 cm and 5.4 cm are recorded at the 1/3- and 2/3-height purlins of Stiff and Flexible cases, respectively, consistent with the maximum OOP displacements of the walls observed at these elevations (see Fig. 14). The V1 numerical model of the Stiff wall shows slightly lower 4.4 cm sliding (−15%) at the 2/3-height purlin, and the Flexible model shows exaggerated sliding at 2/3-height purlins (12.3 cm) and detachment at the top, both consistent with their failure mechanisms. On one note, the cases with one-way bending failure mechanism (experimental walls and the numerical V1 Stiff wall) show that the wall collapse does not require complete purlin detachment, and sliding around 5.25 cm (half of the wall thickness) is sufficient to destabilize the specimens. On another note, the numerical models tend to overestimate the sliding between purlins and the walls, especially in loading runs 12 and above in the Stiff case, and runs 9 and above in the Flexible case, where more considerable sliding is observed in the experiments. This implies

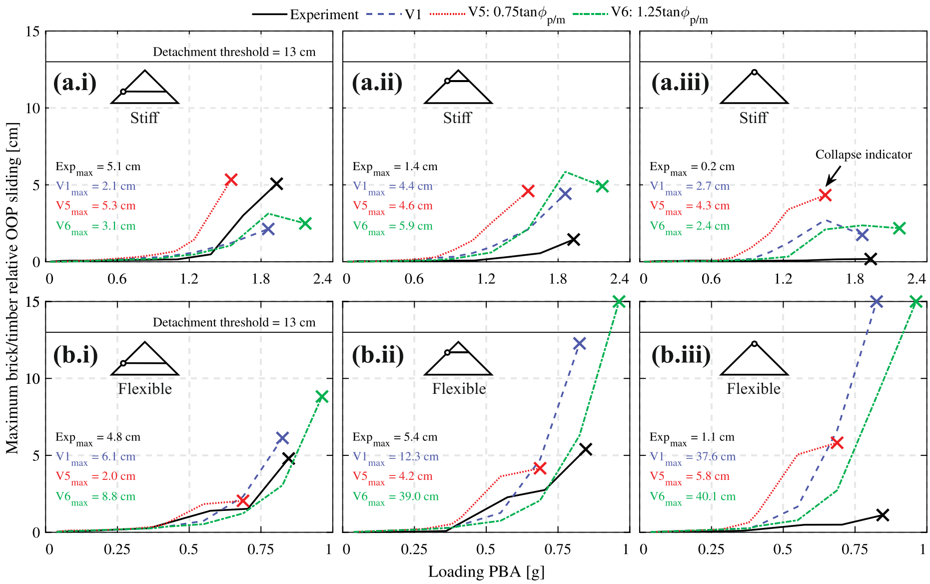

Fig. 15 Maximum out-of-plane sliding recorded between purlins and walls during different loading runs: data recorded at the locations of purlins at 1/3-height (**i**), 2/3-height (ii), and 3/3-height (iii) elevations in the Atiff-Diaphragm (**a**) and Flexible-Diaphragm (**b**) specimens. Experimental data were published only after the competition

that the connection between purlins and walls and other factors influencing its effectiveness, such as stiffness of the loading frame or the accuracy of the vertical loading system in the numerical model, may have caused the difference between numerical and experimental failure mechanisms. This is further investigated in Sections 5.5 and 5.6. It should be noted that while clear purlin-wall detachment is observed during the experiments, they are not reflected in the experimental data shown in Fig. 15. This is because the sensors recording the sliding have been disconnected moments before collapse and purlin-wall detachments. Moreover, the numerical simulations of the Stiff case, especially V1 and V6 with outward bending of the wall, reach the collapse onset while not tracking the full collapse of the wall, including purling detachment, due to numerical convergence issues.

Reducing purlin-wall connection friction in V5 variations expedites collapse by one loading run for both cases. In the V5 Stiff case, reduced friction alters the failure mechanism to one involving a 1/3-height crack due to the inability of the joists to stabilize the wall, resulting in around 5 cm sliding at all purlins. Similarly, in the Flexible case, lower friction accelerates collapse, as the joists fail to return the wall to stability once top drifts reach the wall thickness. Conversely, increasing friction in V6 variations delays collapse by one loading run in both cases. This effect is more pronounced in the Flexible case, where the joists provide continued support until the 1/3-height joint cracks. Given the similarity in purlin behaviors, it is plausible that the V1 Flexible model would have exhibited a similar cracking pattern had the analysis progressed further, potentially through finer solver adjustments. The findings show that while joint properties determine damage onset, collapse ultimately depends on the stability of the walls provided by the purlins. Strengthening purlin-wall connections delays excessive deformations and collapse, especially in the Flexible case. The adopted extreme bounds for the friction coefficients (0.45 and 0.75) show that, due to the lack of detailed experimental investigation into purlin-wall friction, some variability in predicted collapse behavior of the specimens remains plausible. Yet, the original 0.6 friction coefficient is considered adequate for the reference simulation.

5.5 Performance of the numerical loading frame

The OOP accelerations and displacements of the purlins collected from V1 and V7 (with halved frame stiffness) variations for both Stiff and Flexible cases during one loading run before collapse (run 14 for Stiff and 10 for Flexible specimen) and the collapse loading run (15 for Stiff and 11 for Flexible) are compared in Figure 16 against experimental recordings of the same loading runs. The test data are shown with solid black lines, while those of the V1 and V7 numerical models are shown with dashed green lines and dotted red lines, respectively. Final loading runs are depicted as they are assumed to reveal the highest differences between numerical and experimental responses, if any. Both numerical variations closely track the experimental time-histories for their respective cases, showing adequate stiffness of the numerical frame and its ability to replicate the behavior of the frame used in the experiments, up to the collapse of the specimens. Only, the V7 Stiff case progresses further than the V1 specimen (by 5 seconds) and displays a more complete failure mechanism during the collapse loading run (see Fig. 13.c). This indicates that, although the 50% variation of frame stiffness considered here does not affect amplification effects or wall behavior at lower intensities, it may have either influenced deformations under near-collapse conditions or enabled the simulation to pass over any numerical divergence issues. In the case of the latter, it is expected that the V1 specimen could have also shown a similar failure mechanism to V7 should it have progressed further in the last loading run. It should be noted that minor noises in the acceleration data (seen in Fig. 16.acc) may stem from contact interactions between the purlins and the wall through the contact algorithm. These are deemed inconsequential and are not treated in post-processing by means such as filtering.

5.6 Variations in vertical load

The maximum variations (increase) in the axial loads of the trusses connected to different joists during different loading runs of V1 (reference), V8 (with increased truss stiffness), and V9 (trusses replaced with constant loads) simulations for both Stiff and Flexible cases are shown in Figure 17 are compared against the variations in the vertical load of the springs used in the experiments. The data point is calculated by multiplying the stiffness of the vertical loading apparatus by its maximum axial deformation and normalizing the product by its axial load at the start of the dynamic loading run 1. In the experimental data (solid black lines), the deformations directly recorded for springs are used as axial deformations, whereas the numerical data for V1 (shown with dashed blue lines) and V8 (shown with dashed dotted green lines) are calculated using the entire deformation of each truss.

The experimental specimens have experienced as much as 1.5% and 11.1% variations of axial load in the Stiff (up to run 13, until which the data are available) and Flexible tests, respectively, both recorded for the top joist. In the Stiff V1 simulation, while a generally similar trend is observed, the medium and long trusses show slightly higher and lower variations compared to the experimental set-up, respectively, the longest peaking at 2.5% variation. The discrepancies are larger in the Flexible case, where the short and medium numerical trusses show variations almost twice those of the experimental set-up. Perhaps the overturning mechanism of the numerical Flexible specimen, not observed in the experiment, has resulted in larger-than-reality variations of the short and medium trusses close to that of the long truss (9.2%). It should be noted that the spring connected to the top joist in the Flexible experiment shows slightly larger variations compared to the V1 model and as much as the V8 model, suggesting that this spring may have been stiffer than the rest.

The V8 simulations, which feature higher variations due to the use of stiffer trusses, show no differences from the V1 cases regarding collapse loading run or failure mechanism. This indicates that any higher variations in the vertical load during the experiment would not have altered the outcomes of the Stiff or Flexible tests. In contrast, the V9 simulations, where constant vertical loads replace the trusses, reveal distinct behaviors. While the V9 Flexible case mirrors the V1 response, the Stiff V9 wall exhibits a one-way bending failure with an additional crack forming two brick rows above the bottom of the 1/3-height purlin. Moreover, this specimen shows a double curvature one-way bending mechanism (Fig. 13.d) instead of the single curvature one exhibited by the V9 model (Fig. 13.c). This difference is attributed to reduced arching effects caused by the constant vertical loads, lower confinement of the wall, and increase purlin-wall sliding, all of which lead to easier crack formation.

The peak axial deformations (elongation) of the entire loading apparatus connected to each joist are collected from different loading runs of Stiff and Flexible experiments and are compared to those of the V1, V8, and V9 simulations in Fig. 18. A very good match is observed across the data, suggesting that although leading to different variations in vertical

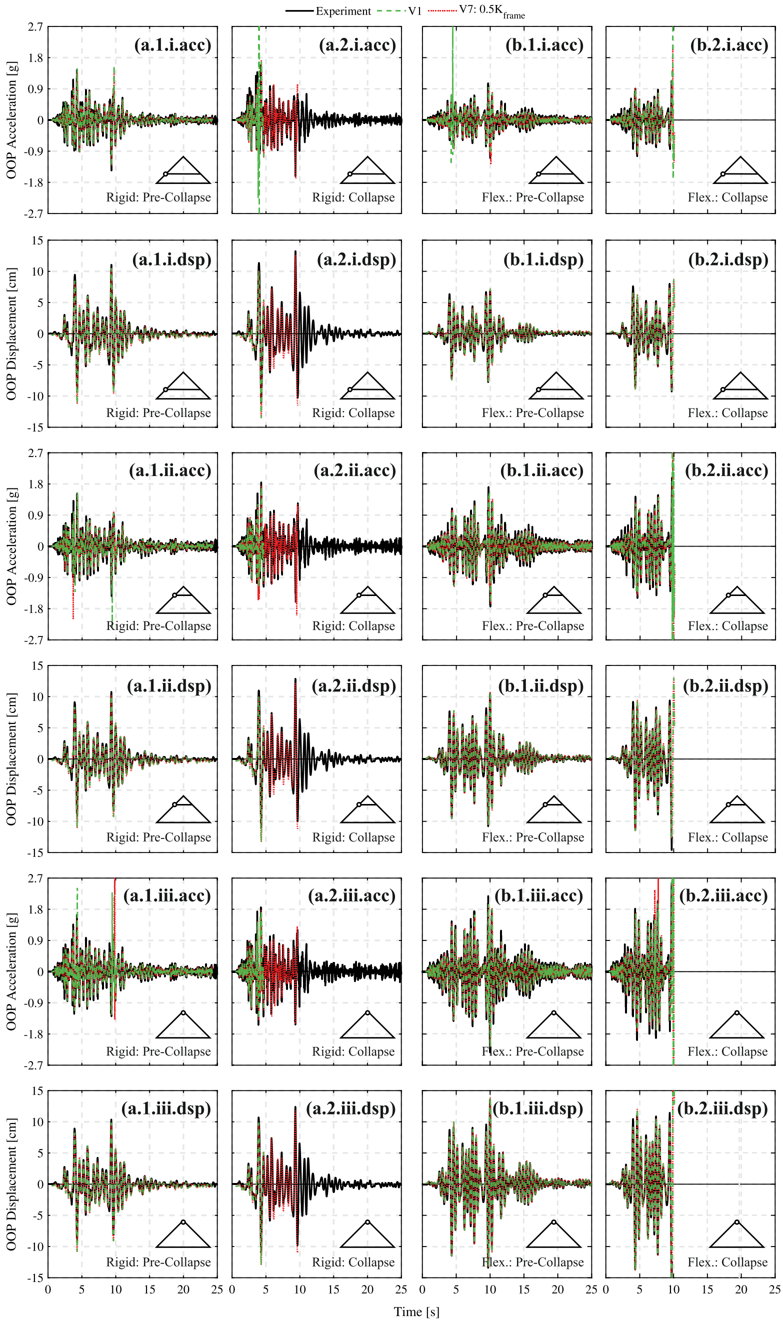

Fig. 16 Purlin motions recorded in the numerical models: acceleration (acc) and displacement (dsp) time histories of the out-of-plane motions recorded for purlins at 1/3-height (**i**), 2/3-height (ii), and 3/3-height (iii) elevations during one loading run prior to collapse (1) and the loading run leading to collapse (2) of reference Stiff-Diaphragm (**a**) and Flexible-Diaphragm (**b**) numerical specimens. Experimental data were only published after the competition

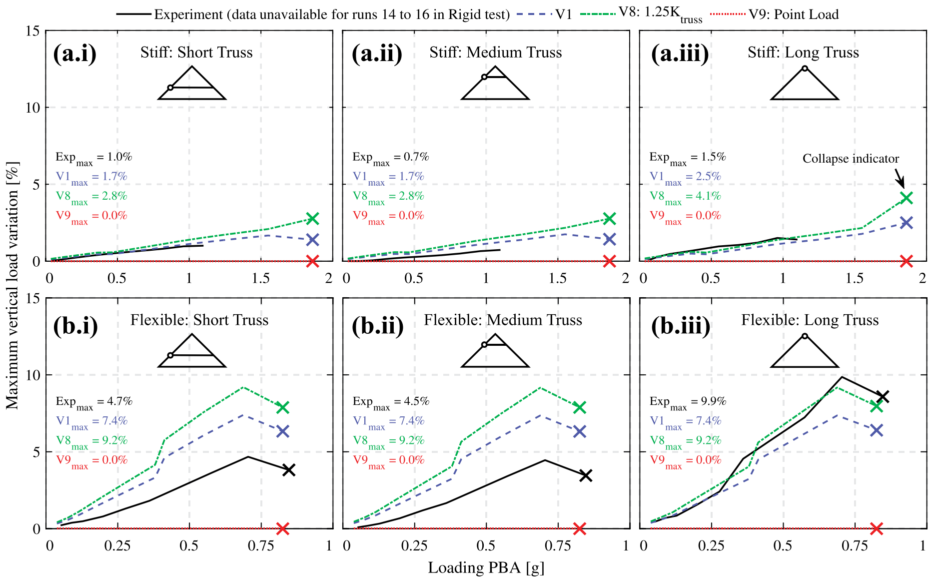

Fig. 17 Maximum variations in the vertical loads applied to the numerical models during different loading runs: trusses connected to 1/3-height (**i**), 2/3-height (ii), and 3/3-height (iii) elevation joists of the Stiff-Diaphragm (**a**) and Flexible-Diaphragm (**b**) specimens. Experimental data were published only after the competition

loads, the spring and rod systems of the experiments have experienced deformations very similar to the numerical trusses. This highlights a key limitation of the assumption made during the experiments, where the rods connected to the springs are assumed to act rigidly. The stiffness of the spring-rod combinations is considered equal to that of the springs (53.5 N/mm) during the tests, and all the deformations of the joists are assumed to be directly transferred to the springs. However, the findings of this section indicate that the flexibility of the rods may have changed (generally reduced) the deformations transmitted to the springs, which in return has led to different variations in the vertical load than had been expected. In other words, the vertical loading system used in the experiments may not have acted as stiff as anticipated. Since the vertical loads in the V9 simulation are assumed to remain constant throughout the analyses (dotted red lines in Fig. 17), such discrepancies are better reflected. Therefore, this variation shows a failure mechanism that is more consistent with the experiment in the Stiff case. For the Flexible case, large drifts disrupt arching effects regardless of vertical load variation, resulting in a mechanism dominated by purlin detachment rather than the vertical load, and hence lower sensitivity to variations in the vertical load.

5.7 Hysteretic response and energy dissipation

The normalized hysteretic force-displacement response and cumulative energy dissipation of V1 (reference, blue dashed lines), V12 (lower damping, red dotted lines), and V13 (higher damping, green dashed dotted lines) variations are compared to the experimental data (solid black lines) for both Stiff and Flexible cases in Fig. 19. Experimental reaction forces are calculated by multiplying the accelerograms of the wall sensors by their contributory masses

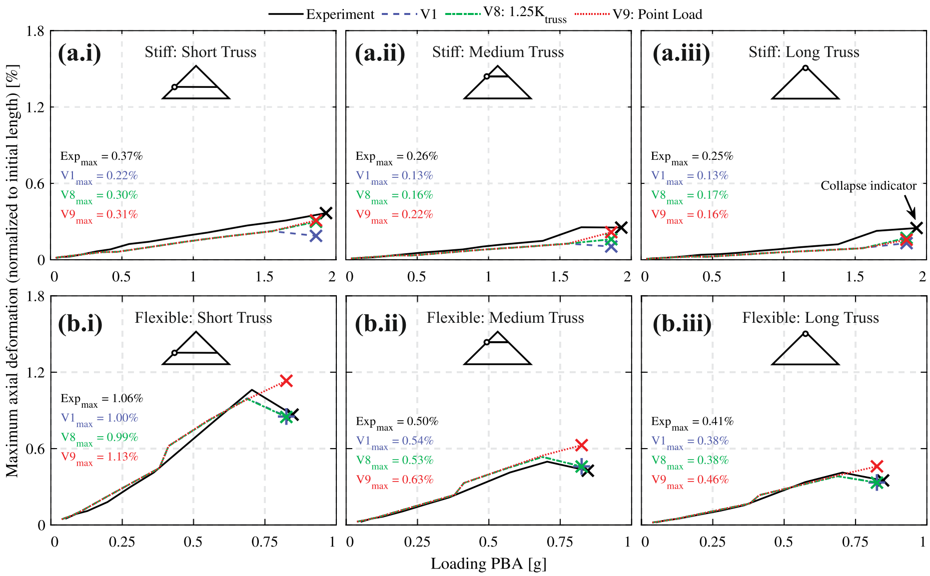

Fig. 18 Maximum axial deformation in the vertical loading trusses of the numerical models during different loading runs: trusses connected to 1/3-height (**i**), 2/3-height (ii), and 3/3-height (iii) elevation joists of the stiff-diaphragm (**a**) and Flexible-diaphragm (**b**) specimens. Experimental data were published after the competition

(see (Sharma et al. 2025)), whereas the numerical reaction forces are the summation of the values directly extracted from boundary points. Hence, they are normalized by the weight of each experimental wall (17.5 kN) and the total weight of each numerical wall and loading set-up (44 kN), respectively, for more straightforward comparison. Displacements are calculated as pure deformations of the walls, i.e., OOP displacements of the control points minus the OOP displacement of the loading frame. For the Flexible case, the control point is set at the 2/3-height elevation for experimental as well as numerical specimens. However, the control point for the Stiff experimental data is assumed at 1/3-height elevation. In contrast, that of the numerical data is taken from 2/3-height elevation, since cracking of the Stiff numerical models occurs at a different location than the experimental wall.

In the experiments, the Stiff case shows a 45% larger peak shear coefficient compared to the Flexible specimen, due to its higher resistance to the adopted boundary conditions. Moreover, this specimen shows a shear response with wide hysteretic loops. In contrast, the Flexible case shows more of a rocking behavior with gradual detachment from the loading set-up, characterized by closed loops and residual displacements with respect to the loading frame at the end of each loading run. Interestingly, both specimens show the same levels of final OOP displacements (as much as the thickness), unaffected by the loading conditions, which results in 110% higher energy dissipation for the Stiff case compared to the Flexible test. This is an expected behavior as, when only the deformation of the wall is considered (without diaphragm motion), both walls have the same rocking response. The V1 numerical models effectively capture the hysteretic response of both cases in terms of stiffness, peak strength (only 15% difference), and maximum displacement, despite their different collapse mechanisms. Although the V1 Stiff model collapses at a 37% lower OOP displacement

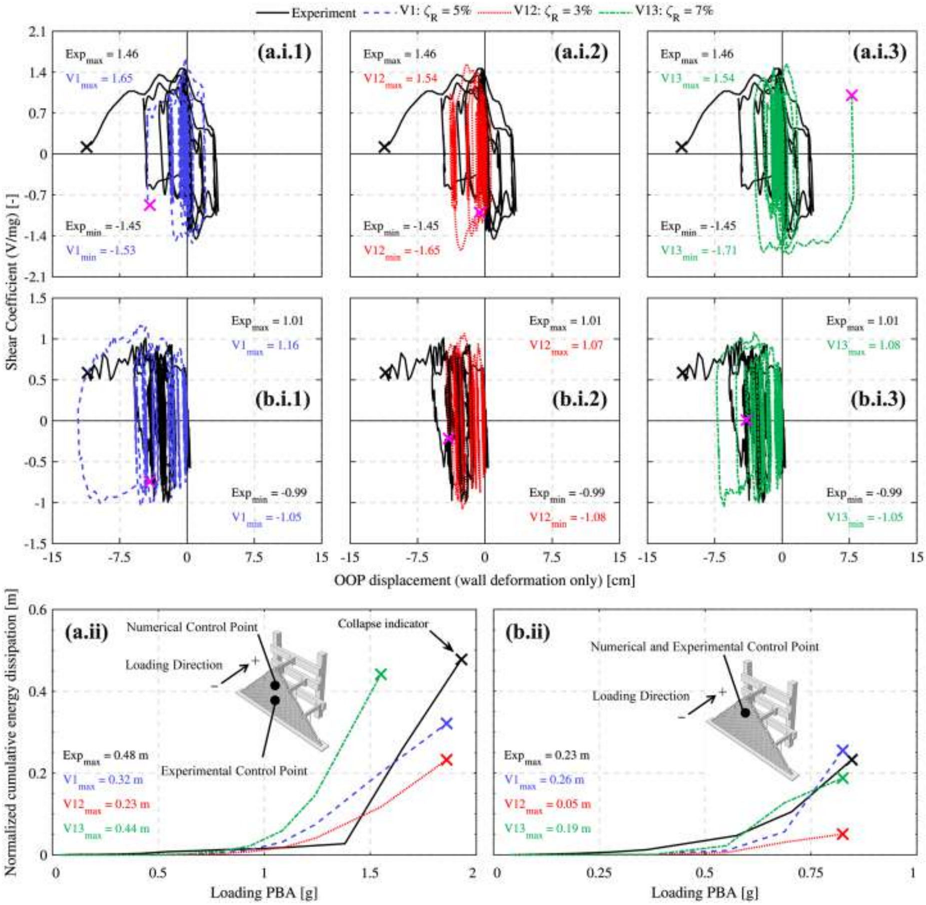

Fig. 19 Hysteretic response of the numerical models: normalized force-displacement curves (**i**) and cumulative energy dissipations after each loading run (ii) for the Stiff-Diaphragm (**a**) and Flexible-Diaphragm (**b**) specimens. Experimental data were published only after the competition. The cross marks indicating collapse in the hysteretic response of the numerical models have been recolored in pink to improve visibility

compared to the experimental wall due to the early termination of its analysis because of numerical convergence issues, it is considered sufficiently representative of the real-world response, as the large displacements are only observed in the collapse and post-collapse state of the experimental wall. The V1 models also replicate well the hysteretic loops and energy dissipations of the experiments, with only the Stiff model showing 36% lower final energy dissipation due to the absence of the last hysteretic loop of the experiment in this model.

In the Stiff case, the V12 variation collapses at the same loading run as V1 but shows slightly lower energy dissipation linked to the delay in the cracking at its base. The V13 variation collapses one run earlier, likely due to over-excitation of higher-frequency deformation modes. Yet, this model shows better energy dissipation than the V1 model, as it can attain 90% larger final OOP displacement. In the Flexible case, both V12 and V13 variations collapse at the same run as V1, with similar overturning mechanisms. However, V12 shows 65% lower OOP displacement and significantly lower energy dissipation due to lower excitation of rigid body motions as a result of lower damping. Due to these differences, the adopted 5% damping ratio is considered to effectively simulate the response of both Stiff and Flexible cases.

6 Conclusions

This paper details the modeling approach adopted for the blind prediction of the OOP dynamic response of unreinforced masonry gables subjected to shake table loading under different boundary conditions. A recent 3D block-based numerical model is utilized for high-fidelity simulation of experiments conducted at the EUCENTRE foundation (Pavia, Italy) within the scope of the ERIES SUPREME blind prediction competition. Two masonry gable walls were tested under multi-step sequences of incremental dynamic OOP loading, with equal or differential motions applied to their top and bottom boundaries. The first is referred to as the Stiff-Diaphragm (or Stiff) specimen, and the second is identified as the Flexible-Diaphragm (of Flexible) specimen. A pair of numerical models, referred to as reference models, is calibrated based on the experimental data published for the competition to represent each wall and its loading set-up. Afterwards, the simulations are extended in a parametric study to accommodate uncertainties inherent in experimental conditions. Numerical outcomes are compared with experimental results released only after the competition to assess the effectiveness of the modeling approach and identify potential refinements for the post-diction phase. The numerical models give the best prediction of collapse mechanisms and loading intensities leading to failure of each specimen, overall achieving the most accurate results among participants. The models also capture key behaviors, including initial stiffness, peak strength, ultimate deformation, hysteretic response, and energy dissipation. The main findings are as follows:

- The reference numerical models replicate the loading intensities causing the collapse of each specimen, but exhibit slightly different failure mechanisms compared to the experiments. Nevertheless, variations in the parametric study effectively capture the failure pattern of the Stiff specimen and improve the simulation of the Flexible collapse.
- The parametric study reveals sensitivity to several factors, with the most influential aspects to be refined in post-diction being the friction coefficient considered for the connections between the loading set-up and the walls, and the apparatus considered for vertical loading application.
- The friction between loading joists and the walls is the key contributor to the stability of the specimens. Low friction values lead to early collapse due to joist detachment or their inability to stabilize the walls during large deformations. High frictions delay collapse, allowing internal wall damage to occur before failure.
- Variations in vertical loads caused by the axial deformation of the loading apparatus can influence the collapse patterns. High-stiffness set-ups impose an excessive increase in vertical loads, leading to confinement and virtual arching effects, which restrict crack openings and uplift. Conversely, low-stiffness setups (e.g., constant concentrated forces) mitigate such limitations.

- Other parameters, including material and damping properties as well as loading direction, show considerable impact on the numerical outcomes. Nonetheless, the settings considered for them in the reference numerical models are already well-representative of the experimental specimens.
- Accurate numerical simulation critically depends on using motions experienced by the specimens. Accordingly, a limitation is noticed as the prediction simulations rely on sample signals extracted from reference runs, rather than actual experimental motions.
- The loading set-up simulated for the models accurately mirrored its experimental counterpart in terms of deformations and accelerations transferred to the specimens. This digital twin offers potential for exploring scenarios beyond those considered in physical tests.

The findings highlight the reliability of the modeling approach proposed by the authors for simulating unreinforced masonry walls with complex geometries and boundary conditions under multi-step OOP dynamic loading. The parametric study underscores the high sensitivity of dynamic OOP responses, necessitating probabilistic approaches for studying dynamic behaviors. The modeling approach offers a robust, resource-efficient complement to experiments, enabling extended insights beyond laboratory constraints. Another publication will focus on refining the models during a post-diction phase based on the points of improvement identified in this paper. Moreover, the re-calibrated models will be applied to simulate a third experiment involving semi-differential boundary motions not included in the competition, as well as to complement the experiments and explore structural scenarios not investigated experimentally.

Acknowledgements All experimental data used as a benchmark in this paper was produced as part of the "ERIES Seismic Out-of-Plane Response of Masonry Gable" project at the EUCENTRE Foundation, Pavia, Italy [23].

Author contributions AG: Conceptualization, Methodology, Software, Validation, Formal analysis, Investigation, Resources, Data Curation, Writing – Original Draft, Writing – Review and Editing, Visualization, Funding acquisition. AMD: Conceptualization, Methodology, Software, Validation, Resources, Writing – Review and Editing, Supervision, Funding acquisition. PBL: Conceptualization, Methodology, Validation, Resources, Writing – Review & Editing, Supervision, Funding acquisition. SdM: Conceptualization, Methodology, Validation, Resources, Writing – Review & Editing, Supervision, Funding acquisition.

Funding This project was supported by the Erasmus+ programme of the European Union under the Staff Mobility Grant for Training. This project has also received funding from the European Union's Horizon 2020 research and innovation programme under the Marie Sklodowska-Curie grant agreement (101029792). This study has been also funded by the STAND4HERITAGE project (new STANDards FOR seismic assessment of built cultural HERITAGE) that has received funding from the European Research Council (ERC) under the European Union's Horizon 2020 research and innovation program (833123) as an Advanced Grant. This work was partially supported by ReLUIS and the Italian Department of Civil Protection, as part of the activity was carried out in the framework of the ReLUIS-DPC Project 2024–2026–Work Package 10 (Masonry structures), Task 10.1.

Data availability The datasets generated during the current study are available from the corresponding author on reasonable request.

Declarations

Conflict of interest The authors have no relevant financial or non-financial interests to disclose.

References

Almeida JP, Beyer K, Brunner R, Wenk T (2020) Characterization of mortar-timber and timber-timber cyclic friction in timber floor connections of masonry buildings. Mater Struct 53:51. https://doi.org/10.1617/s11527-020-01483-y

Bommer JJ, Crowley H, Pinho R, Polidoro B (2015) Selection of acceleration time-series for shake table testing of Groningen masonry building at the EUCENTRE, Pavia. Groningen field seismic hazard and risk assessment project, Pavia, Italy

Boore DM, Bommer JJ (2005) Processing of strong-motion accelerograms: needs, options and consequences. Soil Dyn And Earthquake Eng 25:93–115. https://doi.org/10.1016/j.soildyn.2004.10.007

The British Standard (2003) BS en 338: 2003 - structural timber. Strength Classes

Candeias PX, Costa AC, Mendes N, et al (2016) Experimental assessment of the out-of-plane performance of masonry buildings through shaking table tests. Int J Architectural Heritage 1–28. https://doi.org/10.1080/15583058.2016.1238975

D'Altri AM, de Miranda S, Castellazzi G, Sarhosis V (2018) A 3D detailed micro-model for the in-plane and out-of-plane numerical analysis of masonry panels. Comput Struct 206:18–30. https://doi.org/10.1016/j.compstruc.2018.06.007

D'Altri AM, Messali F, Rots J, et al (2019) A damaging block-based model for the analysis of the cyclic behaviour of full-scale masonry structures. Eng Fract Mech 209:423–48. https://doi.org/10.1016/j.engfracmech.2018.11.046

D'Ayala DF, Paganoni S (2011) Assessment and analysis of damage in L'Aquila historic city centre after 6th April 2009. Bull Of Earthquake Eng 9:81–104. https://doi.org/10.1007/s10518-010-9224-4

Eslami H, Jayasinghe LB, Waldmann D (2021) Nonlinear three-dimensional anisotropic material model for failure analysis of timber. Eng Fail Anal 130:105764. https://doi.org/10.1016/j.engfailanal.2021.105764

European Committee for Standardization (2004) Eurocode, 5: Design of timber structures - part 1-1. Gener - common rules and rules for build

European Committee for Standardization (2005) Eurocode, 3: design of steel structures - part 1-1. Gener Rules And Rules For Build

Frankie TM, Gencturk B, Elnashai AS (2013) Simulation-based fragility relationships for unreinforced masonry buildings. J Struct Eng 139:400–10. https://doi.org/10.1061/(ASCE)ST.1943-541X.0000648

Furiosi A, Damiani N, Rota M, Penna A (2025) Seismic fragility assessment of a multi-span masonry arch bridge using a discontinuum modeling approach. Earthq Eng Struct Dyn 54:3320–40. https://doi.org/10.1002/eqe.70029

Ghezelbash A, D'Altri AM, Sharma S, et al (2024) A block-based numerical strategy for modeling the dynamic out-of-plane behavior of unreinforced brick masonry walls. Meccanica. https://doi.org/10.1007/s11012-024-01899-8

Ghezelbash A, Messali F, Rots JG (2023) Finite element micro-modelling of masonry structures: calibration and analysis challenges. In Engineering Mechanics Institute (EMI) International Conference, Palermo, Italy

Ghezelbash A, Sharma S, D'Altri AM, et al (2025) Challenges in High-Fidelity implicit Block-based numerical simulation of dynamic out-of-plane two-way bending in unreinforced brick masonry walls. Earthq Eng Struct Dyn. https://doi.org/10.1002/eqe.4337

Giaretton M, Dizhur D, Ingham JM (2016) Dynamic testing of as-built clay brick unreinforced masonry parapets. Eng Struct 127:676–85. https://doi.org/10.1016/j.engstruct.2016.09.016

Girardi M, Padovani C, Pellegrini D, Robol L (2021) A finite element model updating method based on global optimization. Mech Syst Signal Process 152:107372. https://doi.org/10.1016/j.ymssp.2020.107372

Graziotti F, Damiani N, Sharma S, et al (2024) Out-of-plane shake-table tests on full-scale URM gables considering different roof configurations (ERIES-SUPREME). Pavia, Italy

Graziotti F, Tomassetti U, Penna A, Magenes G (2016) Out-of-plane shaking table tests on URM single leaf and cavity walls. Eng Struct 125:455–70. https://doi.org/10.1016/j.engstruct.2016.07.011

Graziotti F, Tomassetti U, Sharma S, et al (2019) Experimental response of URM single leaf and cavity walls in out-of-plane two-way bending generated by seismic excitation. Constr Build Mater 195:650–70. https://doi.org/10.1016/j.conbuildmat.2018.10.076

Graziotti F, Toninelli P, Solenghi M, et al (2019) Numerical simulation of the nonlinear earthquake response of a monitored URM school building. In 7th ECCOMAS Thematic Conference on Computational Methods in Structural Dynamics and Earthquake Engineering (COMPDYN), Crete, Greece

Griffith MC, Lam NTK, Wilson JL, Doherty K (2004) Experimental investigation of unreinforced Brick masonry Walls in Flexure 130:423–32.

Hendry EAW (2001) Masonry walls: materials and construction. Constr Build Mater 15:323–30. https://doi.org/10.1016/S0950-0618(01)00019-8

Hibbitt D, Karlsson B, Sorensen P (2011) Abaqus/CAE User's manual. Dassault Systèmes SE, USA

Hilber HM, Hughes TJ, Talor RL (1977) Improved numerical dissipation for Time integration algorithms in structural dynamics. Earthq Eng Struct Dyn 282–92

Jafari S, Esposito R (2016) Material tests for the characterisation of replicated calcium silicate Brick masonry. Delft, Netherlands

Jafari S, Esposito R, Rots JG (2019) From brick to element: Investigating the mechanical properties of calcium silicate masonry 596–604

Kesavan P, Menon A (2022) Investigation of in-plane and out-of-plane interaction in unreinforced masonry piers by block-based micro-modeling. Structures 46:1327–44. https://doi.org/10.1016/j.istruc.2022.10.105

Kesavan P, Menon A (2023) A macro-element with bidirectional interaction for seismic analysis of unreinforced masonry walls. Earthq Eng Struct Dyn 52:1740–61. https://doi.org/10.1002/eqe.3841

Lee J, Fenves GL (1998) Plastic-damage Model for cyclic loading of concrete structures. J Eng Mech 124:892–900.

Lourenço PB (2000) Anisotropic softening Model for masonry plates and shells 126:1008–16

Lourenço PB (2004) Current experimental and numerical issues in masonry research. In Proceedings of the 13th International Brick and Block Masonry Conference, Amsterdam, The Netherlands

Lubliner J, Oliver J, Oller S, Oñate E (1989) A plastic-damage model for concrete. Int J Solids Struct 25:299–326. https://doi.org/10.1016/0020-7683(89)90050-4

Macorini L, Izzuddin BA (2011) A non-linear interface element for 3D mesoscale analysis of brick-masonry structures. Int J Numer Methods Eng 85:1584–608. https://doi.org/10.1002/nme.3046

Malomo D, DeJong MJ (2022) A macro-distinct element Model (M-DEM) for simulating in-plane/out-of-plane interaction and combined failure mechanisms of unreinforced masonry structures. Earthq Eng Struct Dyn 51:793–811. https://doi.org/10.1002/eqe.3591

Malomo D, Pinho R, Penna A (2020) Numerical modelling of the out-of-plane response of full-scale brick masonry prototypes subjected to incremental dynamic shake-table tests. Eng Struct 209:110298. https://doi.org/10.1016/j.engstruct.2020.110298

Milani G, Valente M, Alessandri C (2018) The narthex of the church of the nativity in Bethlehem: a non-linear finite element approach to predict the structural damage. Comput Struct 207:3–18. https://doi.org/10.1016/j.compstruc.2017.03.010

Mirra M, Damiani N, Sharma S, et al (2025) Definition of differential seismic input motions for out-of-plane dynamic testing of unreinforced masonry gable walls considering different roof configurations. Structures 79:109419. https://doi.org/10.1016/j.istruc.2025.109419

Mirra M, Ravenshorst G, van de Kuilen J (2020) Experimental and analytical evaluation of the in-plane behaviour of as-built and strengthened traditional wooden floors. Eng Struct 211:110432. https://doi.org/10.1016/j.engstruct.2020.110432

Mohyeddin A, Goldsworthy HM, Gad EF (2013) Fe modelling of RC frames with masonry infill panels under in-plane and out-of-plane loading. Eng Struct 51:73–87. https://doi.org/10.1016/j.engstruct.2013.01.012

Moon L, Dizhur D, Senaldi I, et al (2014) The demise of the URM building stock in Christchurch during the 2010–2011 canterbury earthquake sequence. Earthquake Spectra 30:253–76

Moshfeghi A, Smyrou E, Arslan O, Engin Bal I (2024) Out-of-plane shake table tests on solid masonry walls with timber floors. Structures 66:106815. https://doi.org/10.1016/j.istruc.2024.106815

Nie Y, Sheikh A, Visintin P, Griffith M (2023) A robust computational strategy for failure prediction of masonry structures using an improved multi-surface damage-plastic based interface model. Int J Numer Methods Eng 124:2498–528. https://doi.org/10.1002/nme.7218

Noor-E-Khuda S (2021) An explicit finite-element modeling Method for masonry Walls using continuum Shell element. J Architectural Eng 27. https://doi.org/10.1061/(ASCE)AE.1943-5568.0000518

Noor-E-Khuda S, Dhanasekar M, Thambiratnam DP (2016) An explicit finite element modelling method for masonry walls under out-of-plane loading. Eng Struct 113:103–20. https://doi.org/10.1016/j.engstruct.2016.01.026

Oktiovan YP, Davis L, Wilson R, et al (2024) Simplified micro-modeling of a masonry cross-vault for seismic assessment using the distinct element method. Int J Architectural Heritage 18:1915–48. https://doi.org/10.1080/15583058.2023.2277328

Oktiovan YP, Messali F, Pulatsu B, et al (2024) A contact-based constitutive model for the numerical analysis of masonry structures using the distinct element method. Comput Struct 303:107499. https://doi.org/10.1016/j.compstruc.2024.107499

Oyarzo-Vera C, Griffith MC (2009) The mw 6.3 Abruzzo (Italy) earthquake of april 6th, 2009: on site observations. Bull Of The New Zealand Soc For Earthquake Eng 42:302–07

Page AW (1991) The Newcastle earthquake - behaviour of masonry structures. Masonry Int 5:11–18

Penna A, Morandi P, Rota M, et al (2014) Performance of masonry buildings during the emilia 2012 earthquake. Bull Of Earthquake Eng 12:2255–73. https://doi.org/10.1007/s10518-013-9496-6

Penner O, Elwood KJ (2016a) Out-of-plane dynamic stability of unreinforced masonry Walls in one-way bending: parametric study and assessment guidelines. Earthquake Spectra 32:1699–723. https://doi.org/10.1193/011715EQS011M

Penner O, Elwood KJ (2016b) Out-of-plane dynamic stability of unreinforced masonry Walls in one-way bending: shake table testing. Earthquake Spectra 32:1675–97. https://doi.org/10.1193/011415EQS009M

Rots JG, Messali F, Esposito R, et al (2016) Thematic keynote computational modelling of masonry with a view to Groningen induced seismicity. In 10th International Conference on Structural Analysis of Historical Constructions, Leuven, Belgium

Scacco J, Ghiassi B, Milani G, Lourenço PB (2020) A fast modeling approach for numerical analysis of unreinforced and FRCM reinforced masonry walls under out-of-plane loading. Compos B Eng 180:107553. https://doi.org/10.1016/j.compositesb.2019.107553

Selby RG, Vecchio FJ (1993) Three-dimensional constitutive relations for reinforced concrete. University of Toronto

Sharma S, Damiani N, Bertassi M, et al (2025) Experimental data from out-of-plane shake-table tests on unreinforced masonry gables. Earthquake Spectra. https://doi.org/10.1177/87552930251378248

Sharma S, Silva LC, Graziotti F, et al (2021) Modelling the experimental seismic out-of-plane two-way bending response of unreinforced periodic masonry panels using a non-linear discrete homogenized strategy. Eng Struct 242:112524. https://doi.org/10.1016/j.engstruct.2021.112524

Sharma S, Tomassetti U, Graziotti F, Magenes G (2021) Simplified methodologies for assessing the out-of-plane two-way bending seismic response of unreinforced brick masonry walls: lessons from recent experimental studies. Structures 33:2839–54. https://doi.org/10.1016/j.istruc.2021.03.121

Simsir CC, Aschheim MA Abrams D (2004) Out-of-plane dynamic response of unreinforced bearing walls attached to flexible diaphragms. In Proceedings of 13th World Conference on Earthquake Engineering

Sorrentino L, D'Ayala D, de Felice G, et al (2016) Review of out-of-plane seismic assessment techniques applied to existing masonry buildings. Int J Architectural Heritage 1–20. https://doi.org/10.1080/15583058.2016.1237586

Tomassetti U, Correia AA, Candeias PX, et al (2019) Two-way bending out-of-plane collapse of a full-scale URM building tested on a shake table. Bull Of Earthquake Eng 17:2165–98. https://doi.org/10.1007/s10518-018-0507-5

Tondelli M, Beyer K, DeJong M (2016) Influence of boundary conditions on the out-of-plane response of brick masonry walls in buildings with RC slabs. Earthq Eng Struct Dyn 45:1337–56. https://doi.org/10.1002/eqe.2710

Vaculik J, Griffith MC (2018) Out-of-plane shaketable testing of unreinforced masonry walls in two-way bending. Bull Of Earthquake Eng 16:2839–76

Vanin F, Penna A, Beyer K (2020) A three-dimensional macroelement for modelling the in-plane and out-of-plane response of masonry walls. Earthq Eng Struct Dyn 49:1365–87. https://doi.org/10.1002/eqe.3277

Weyler R, Oliver J, Sain T, Cante JC (2012) On the contact domain method: a comparison of penalty and Lagrange multiplier implementations. Comput Methods Appl Mech Eng 205-208:68–82. https://doi.org/10.1016/j.cma.2011.01.011

Xie Z, Sousamli M, Messali F, Rots JG (2021) A sub-stepping iterative constitutive model for cyclic cracking-crushing-shearing in masonry interface elements. Comput Struct 257:106654. https://doi.org/10.1016/j.compstruc.2021.106654

Yue J, Fafitis A, Qian J (2010) On the kinematic coupling of 1D and 3D finite elements: a structural model. Interact And Multiscale Mech 3:192–211. https://doi.org/10.12989/imm.2010.3.2.192

Authors and Affiliations

Amirhossein Ghezelbash[1] · **Antonio Maria D'Altri**[2] · **Paulo B. Lourenço**[3] · **Stefano de Miranda**[2]

✉ Amirhossein Ghezelbash
a.ghezelbash@tudelft.nl

1 Faculty of Civil Engineering and Geosciences – Delft University of Technology, Delft, The Netherlands

2 Department of Civil, Chemical, Environmental, and Materials Engineering – University of Bologna, Bologna, Italy

3 ISISE, Department of Civil Engineering – University of Minho, Guimarães, Portugal